

11-14-2017

Mechanistic Modeling of Nanoparticle-stabilized Supercritical CO₂ Foams and its Implication in Field-scale EOR Applications

Doris Patricia Ortiz Maestre

Louisiana State University and Agricultural and Mechanical College

Follow this and additional works at: https://digitalcommons.lsu.edu/gradschool_theses



Part of the [Nanoscience and Nanotechnology Commons](#), [Other Engineering Commons](#), and the [Petroleum Engineering Commons](#)

Recommended Citation

Ortiz Maestre, Doris Patricia, "Mechanistic Modeling of Nanoparticle-stabilized Supercritical CO₂ Foams and its Implication in Field-scale EOR Applications" (2017). *LSU Master's Theses*. 4347.

https://digitalcommons.lsu.edu/gradschool_theses/4347

This Thesis is brought to you for free and open access by the Graduate School at LSU Digital Commons. It has been accepted for inclusion in LSU Master's Theses by an authorized graduate school editor of LSU Digital Commons. For more information, please contact gradetd@lsu.edu.

**MECHANISTIC MODELING OF NANOPARTICLE-STABILIZED
SUPERCRITICAL CO₂ FOAMS AND ITS IMPLICATION IN
FIELD-SCALE EOR APPLICATIONS**

A Thesis

Submitted to the Graduate Faculty of the
Louisiana State University and
Agricultural and Mechanical College
in partial fulfillment of the
requirements for the degree of
Master of Science
in

The Department of Petroleum Engineering

by
Doris Patricia Ortiz Maestre
B.S., Universidad de América, Bogotá, 2011
November 2017

ACKNOWLEDGEMENTS

I would first like to thank my thesis advisor Dr. Seung Kam of the Craft and Hawkins Department of Petroleum Engineering at Louisiana State University, whose expertise, understanding, guidance and support made it possible for me to work on a challenging topic that was of great interest to me. I am glad to know that I was able to learn from him not only technical skills, but also essential professional competences, like teamwork, responsibility, commitment, organization and problem solving, without which my academic goals could not have been achieved. Those skills and competences will allow me to develop a successful career in my near future.

I would also like to thank Mohammad Izadi, my research fellow, who steered me in the right direction whenever I needed it. His patience and commitment helped me to make a tremendous progress in my research project during all this time.

I must express my very profound gratitude to my family for providing me unconditional support and continuous encouragement throughout this process. They were my motivation and inspiration.

I would like to thank my committee members, Dr. Ipsita Gupta and Dr. Paulo Waltrich for their time and advice. With their challenging questioning, I was encouraged to assess and improve my work.

Computer Modeling Group (CMG) for the reservoir simulation software that has made available for the successful development of this study.

Finally, I am grateful to my LSU classmates and friends who supported me in every aspect of my academic life. They were always there in the easy and difficult moments. Last but not least, I want to thank LSU alma mater, where I learned to love purple and live gold.

TABLE OF CONTENTS

| | |
|---|------|
| ACKNOWLEDGEMENTS..... | ii |
| LIST OF TABLES..... | iv |
| LIST OF FIGURES..... | v |
| ABSTRACT..... | viii |
| 1. INTRODUCTION..... | 1 |
| 1.1 Gas Injection EOR..... | 1 |
| 1.2 Fundamentals of Foam EOR..... | 2 |
| 1.3 Nanoparticle-stabilized Foam EOR..... | 5 |
| 1.4 Experimental Study of Nanoparticle-stabilized Foam EOR..... | 7 |
| 2. OBJECTIVES..... | 9 |
| 3. METHODOLOGY..... | 11 |
| 4. RESULTS..... | 15 |
| 4.1 Model fit to small-scale lab coreflood data..... | 15 |
| 4.1.1 Construction of fractional flow curves..... | 16 |
| 4.1.2 Fit of mechanistic foam model to the data..... | 18 |
| 4.1.3 Implication in displacement efficiency..... | 23 |
| 4.2 Application to the field-scale treatment..... | 25 |
| 4.2.1 Field description..... | 25 |
| 4.2.2 Comparison of different injection scenarios..... | 27 |
| 5. CONCLUSIONS AND RECOMMENDATIONS..... | 30 |
| REFERENCES..... | 32 |
| APENDIX A: PRODUCTION RATE AND CUMULATIVE RECOVERY AT THE END OF 9 YEARS OF INJECTION FOR 13 SIMULATION SCENARIOS..... | 38 |
| APENDIX B: REMAINING OIL SATURATION AT THE END OF 9 YEARS OF INJECTION FOR 13 SIMULATION SCENARIOS..... | 45 |
| VITA..... | 50 |

LIST OF TABLES

| | |
|---|----|
| Table 1. Summary of rock and fluid properties as well as model parameters used in this study..... | 19 |
| Table 2. Simulation input for reservoir and fluid properties for CO ₂ , CO ₂ and water, CO ₂ and nanoparticle solutions, and CO ₂ and surfactant solutions..... | 26 |
| Table 3. Scenarios to evaluate injection of gas, gas and water (no foam), nanoparticle stabilized foams, and surfactant foams..... | 29 |
| Table 4. Summary of the results from 13 different 9-year injection scenarios in terms of cumulative oil recovery, remaining oil saturation and sweep efficiency..... | 30 |

LIST OF FIGURES

| | | |
|------------|--|----|
| Figure 1. | Steady-state pressure contours during the flow of strong foams in a 2-ft long sandpack showing both high-quality regime and low-quality regime... | 4 |
| Figure 2. | Three-dimensional foam rheology surface that represents three different foam states in porous media such as weak-foam, strong-foam and intermediate states..... | 4 |
| Figure 3. | Experimental setup for CO ₂ foam experiments with nanoparticles at room temperature (T = 77 °F)..... | 8 |
| Figure 4. | Steady-state pressure-gradient (∇p) responses in a range of injection rates and injection foam qualities..... | 8 |
| Figure 5. | Lisama Field information to be used for simulation testing in this study..... | 10 |
| Figure 6. | Experimental data redrawn from Horjen (2015) with and without foams, showing the steady-state pressure gradient as a function of gas and liquid velocities..... | 15 |
| Figure 7. | Construction of fractional flow curve to estimate supercritical CO ₂ -brine two-phase relative permeability functions at three different total injection rates..... | 16 |
| Figure 8. | Determination of CO ₂ -brine (no foam) relative permeability curves by making a fit to the fractional flow curve..... | 17 |
| Figure 9. | Construction of fractional flow curves to fit nanoparticle-stabilized supercritical CO ₂ foam experimental data at three different total injection rates..... | 18 |
| Figure 10. | Mechanistic foam model fit to experimental data in Horgen (2015): (a) fit to three foam states, (b) fit to pressure contours showing two strong-foam flow regimes, (c) shear-thinning and shear-thickening parameters determination, and (d) additional pressure contours from σ_H and σ_L in the strong-foam state..... | 20 |
| Figure 11. | Model fit to experimental data for three foam states and two strong-foam flow regimes at different mobilization pressure gradient..... | 21 |
| Figure 12. | Model fit to experimental data for three foam states and two strong-foam flow regimes at different maximum trapped gas saturation..... | 22 |

| | | |
|--------------|---|----|
| Figure 13. | Construction of fractional flow solutions in a wide range of MRF values: (a) fractional flow curves and (b) resulting saturation profiles at the dimensionless time of 0.2..... | 23 |
| Figure 14. | Complicated fractional flow curves from bubble-population-balance mechanistic modeling: (a) fractional flow curves showing three different foam states at $q_t = 2, 3$, and 4 cc/min, (b) corresponding changes in terms of MRF vs. S_w and (c) f_w vs. MRF..... | 24 |
| Figure 15. | Two-dimensional grid system of Mugrosa formation in Lisama Field for field-scale simulations in this study..... | 27 |
| Figure A.1. | Evaluation of supercritical CO ₂ flooding, scenario 1: (a) production rates and (b) cumulative production..... | 38 |
| Figure A.2. | Evaluation of supercritical CO ₂ and water co-injection (MRF = 1), scenario 2: (a) production rates and (b) cumulative production..... | 38 |
| Figure A.3. | Evaluation of supercritical CO ₂ and nanoparticle solution co-injection (MRF = 10), scenario 2a: (a) production rates and (b) cumulative production..... | 39 |
| Figure A.4. | Evaluation of supercritical CO ₂ and surfactant solution co-injection (MRF = 100), scenario 2b: (a) production rates and (b) cumulative production..... | 39 |
| Figure A.5. | Evaluation of supercritical CO ₂ and water co-injection (MRF = 1), scenario 3: (a) production rates and (b) cumulative production..... | 40 |
| Figure A.6. | Evaluation of supercritical CO ₂ and nanoparticle solution co-injection (MRF = 10), scenario 3a: (a) production rates and (b) cumulative production..... | 40 |
| Figure A.7. | Evaluation of supercritical CO ₂ and surfactant solution co-injection (MRF = 100), scenario 3b: (a) production rates and (b) cumulative production..... | 41 |
| Figure A.8. | Evaluation of supercritical CO ₂ and water co-injection (MRF = 1), scenario 4: (a) production rates and (b) cumulative production..... | 41 |
| Figure A.9. | Evaluation of supercritical CO ₂ and nanoparticle solution co-injection (MRF = 10), scenario 4a: (a) production rates and (b) cumulative production..... | 42 |
| Figure A.10. | Evaluation of supercritical CO ₂ and surfactant solution co-injection (MRF = 100), scenario 4b: (a) production rates and (b) cumulative production..... | 42 |

| | | |
|--------------|---|----|
| Figure A.11. | Evaluation of supercritical CO ₂ and water co-injection (MRF = 1), scenario 5: (a) production rates and (b) cumulative production..... | 43 |
| Figure A.12. | Evaluation of supercritical CO ₂ and nanoparticle solution co-injection (MRF = 10), scenario 5a: (a) production rates and (b) cumulative production..... | 43 |
| Figure A.13. | Evaluation of supercritical CO ₂ and surfactant solution co-injection (MRF = 100), scenario 5b: (a) production rates and (b) cumulative production..... | 44 |
| Figure B.1. | Saturation profiles of scenario 1 (Supercritical CO ₂ flooding)..... | 45 |
| Figure B.2. | Saturation profiles of scenarios 2 (MRF = 1), 2a (MRF = 10) and 2b (MRF = 100)..... | 46 |
| Figure B.3. | Saturation profiles of scenarios 3 (MRF = 1), 3a (MRF = 10) and 3b (MRF = 100)..... | 47 |
| Figure B.4. | Saturation profiles of scenarios 4 (MRF = 1), 4a (MRF = 10) and 4b (MRF = 100)..... | 48 |
| Figure B.5. | Saturation profiles of scenarios 5 (MRF = 1), 5a (MRF = 10) and 5b (MRF = 100)..... | 49 |

ABSTRACT

Previous experimental studies show that nanoparticle-stabilized supercritical CO₂ foams (or, NP CO₂ foams) can be applied as an alternative to surfactant foams, in order to reduce CO₂ mobility in gas injection enhanced oil recovery (EOR). These nanoparticles, if chosen correctly, can be an effective foam stabilizer attached at the fluid interface in a wide range of physicochemical conditions.

By using NP CO₂ foam experiments available in the literature, this study performs two tasks: (i) presenting how a mechanistic foam model can be used to fit experimental data and determine required model parameters, and (ii) investigating the sweep efficiency in a condition similar to Lisama Field, in Colombia, by using relevant gas mobility reduction data in CMG-STARS simulations, contrasting NP CO₂ foams to surfactant foams in both dry and wet foam injection methods.

The results show how the model can successfully reproduce coreflood experimental data, creating three different foam states (weak-foam, strong-foam and intermediate states) and two steady-state strong-foam regimes (high-quality and low-quality regimes). When the gas mobility reduction factors ranging up to 10 from the model fit are applied in the field-scale simulations, the use of nanoparticles improves oil recovery compared to gas-water co-injection, but not as efficient as successful surfactant foam injection does. This implies that although nanoparticle-stabilized foams do provide some benefits, there still seems some room to improve stability and strength of resulting foams.

1. INTRODUCTION

1.1 Gas injection EOR

Worldwide energy consumption, especially petroleum and other liquid fuels, is estimated to rise from 90 million barrels per day (b/d) in 2012 to 100 million b/d in 2020, and 121 million b/d in 2040 (U.S. Energy Information Administration, 2016). In consequence, there is an increased necessity of adding hydrocarbon reserves to the world's energy resources. An important strategy to meet the goal is incrementing the recovery factor from existing reservoirs. Normally, new strategies to reduce remaining oil saturation from the reservoir start after a waterflooding process in the field life. One of the enhanced oil recovery (EOR) methods, most commonly applied around the world, is the injection of gas into the reservoir (Manrique et al., 2010). Carbon dioxide (CO₂) has been frequently used in non-hydrocarbon gas injection projects for enhanced oil recovery (EOR) worldwide, including the Permian Basin in the U.S. (Manrique et al., 2010). According to the Oil and Gas Journal (2016), there were 133 active CO₂ injection projects globally in 2016, of which 83% were developed in sandstone reservoirs and the remaining 17% in carbonate reservoirs. The extensive application of CO₂ injection confirms that it is a promising method for increasing oil recovery.

The role of CO₂ in EOR processes is to serve as a miscible or immiscible displacing agent depending on the reservoir conditions and oil composition (El-diasty and Aly, 2015). Designing injection strategies, modeling and forecasting reservoir performance, and optimizing production management are the crucial steps for the successful application of CO₂ injection. Reservoir

conditions are also important to determine the applicability of CO₂ injection, because they affect thermodynamic properties and miscibility.

In spite of the contribution that gas injection has made to the oil production in many fields globally, several challenges have been encountered in the field applications such as, for example, gas supply, minimum gas miscibility pressure, surface equipment constraints, reservoir heterogeneity and high gas/oil mobility ratio (Kang et al., 2014). Reservoir heterogeneity and high gas/oil mobility ratio are the main causes of low sweep efficiency during gas injection together with gravity segregation (Lake, 1989).

1.2 Fundamentals of Foam EOR

The ability of foam to reduce gas mobility has led to its suggested application in a number of production processes, including gas flooding, steam flooding, and certain well-treatment techniques such as gas blockage by using foams to reduce gas coning (Hanssen and Dalland, 1990). Foam as a dispersion of gas phase (for example, hydrocarbon gas, nitrogen, or carbon dioxide among many) in a surfactant-laden liquid phase presents a specialized structure in which the gas phase is separated by thin liquid films called “lamellae” (Hirasaki, 1989). Upon creation, the presence of lamellae causes the reduction in gas mobility because they block part of the pore network and divert the subsequent gas phase into smaller pores, improving sweep efficiency (Friedmann et al., 1991). The number of thin liquid films present in the foam structure determines “foam texture”. Foam texture, which is the number of lamellae in a unit volume (inversely proportional to the size of bubbles), is a key to understanding the rheological properties of foam (Afsharpoor, 2010). “Strong foam” is referred to as a fine-textured foam with relatively high resistance to flow (or high pressure gradient), while “weak foam” is referred to as a coarse-textured foam with relatively low resistance to flow (or low pressure gradient). A region with large amount

of water accumulated, called Plateau border, is formed at the junction of foam films satisfying a certain geometric constraint (120° between films in two-dimensional, and 109.5° between films in three-dimensional space) (Schramm, 1994).

“Foam quality” is another important measure that expresses gas volume fraction in the whole foam mixture (gas and liquid together), i.e., the ratio of gas volume to total foam volume at a given pressure and temperature (Grundmann and Lord, 1983). In addition to foam texture, the flow properties of foam depend on foam quality (Skoreyko et al., 2011).

Suppose strong foams (or, fine-textured foams in terms of foam texture) are obtained. Then, foam quality is a key aspect for understanding transport behavior (i.e., pressure gradient (∇P) vs. flow rate (q)) of foam flow. Osterloh and Jante (1992) experimentally demonstrated that at relatively high foam qualities (or dry foams), the pressure drop during foam flow is nearly independent of gas flow rate, while at relatively low foam qualities (or wet foams), the pressure drop is nearly independent of liquid flow rate (as shown in Fig. 1), which later studies called the high-quality regime and the low-quality regime, respectively, of strong-foam state (Alvarez et al., 2001; Kam and Rossen, 2003; Dholkawala et al., 2007). The high-quality and low-quality regimes are separated by a threshold foam quality denoted by f_g^* (For example, f_g^* in Fig. 1 is about 0.94).

In order to investigate the transition from weak-foam to strong-foam state (often referred to as “(strong) foam generation”, Gauglitz et al. (2002) performed a wide range of foam-generation experiments, the results of which are shown schematically in Fig. 2. They found three distinct foam states (weak-foam state at low ∇P , strong-foam state at high ∇P , and an unstable intermediate foam state in between), and a sudden dramatic change from low ∇P to high ∇P state associated with foam generation (that is, no other than a discontinuous jump from the weak-foam

to strong-foam state). The change in ∇P (i.e., z axis) along the S-shaped curve, which is represented by a slice of the 3D surface in the vertical direction, is proportional to the change in foam texture (n_f) and inversely proportional to gas mobility ($\frac{k_{rg}}{\mu_g}$) in the presence of foam (Kam and Rossen, 2003; Kam et al., 2007).

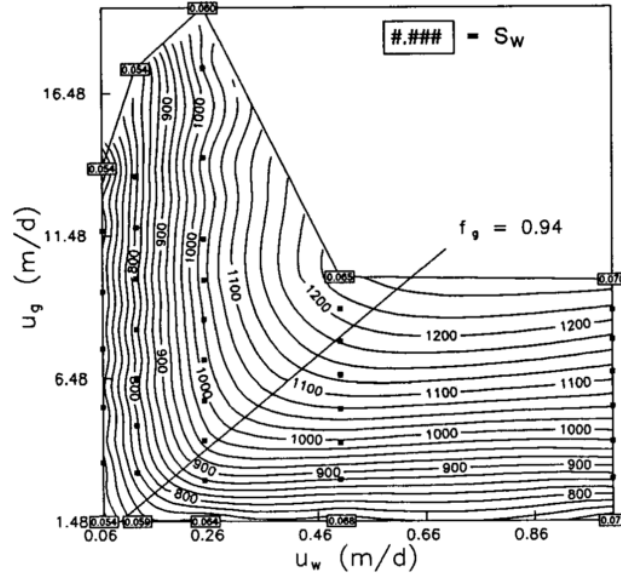


Fig. 1. Steady-state pressure contours during the flow of strong foams in a 2-ft long sandpack (Osterloh and Jante, 1992) showing both high-quality regime and low-quality regime

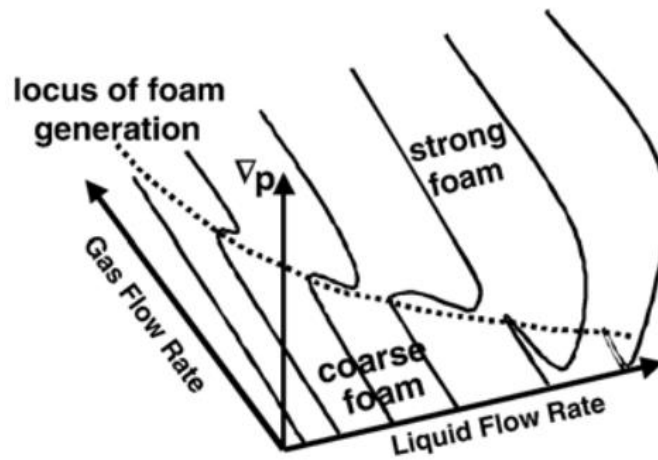


Fig. 2. Three-dimensional foam rheology surface that represents three different foam states in porous media such as weak-foam, strong-foam and intermediate states (Gauglitz et al., 2002)

During foam flow in porous media, dynamic mechanisms allow bubbles to be created or destroyed in situ. As a result, the bubble population reflected by foam texture (n_f) changes constantly as a function of space and time. Such a behavior can be captured in the mechanistic foam modeling by putting lamella creation and coalescence mechanisms together.

Lamellae creation is based on three main mechanisms identified by previous studies such as snap-off, lamellae mobilization-and-division, and leave-behind. Details of these mechanisms can be found elsewhere (Ransohoff and Radke, 1988; Kam and Rossen, 2003). It should be noted that the three foam states presented in Fig. 2 are more relevant to the lamella mobilization and division mechanism in homogeneous media, while the snap-off mechanism, that requires fluctuations in capillary pressure, is more relevant to a medium with heterogeneity.

Lamella coalescence is governed by capillary pressure (P_c). Among many, Khatib et al. (1988) experimentally demonstrated that there is a threshold value of capillary pressure (called limiting capillary pressure, P_{c*}) above which lamella cannot survive. The threshold water saturation that corresponds to P_{c*} in the capillary pressure curve is called limiting water saturation (S_w^*) below which lamella cannot survive either.

1.3 Nanoparticle-stabilized Foam EOR

Although surfactants have been commonly used in EOR applications, the use of nanoparticles is a new emerging technology due to their ability to stay at the interface and reduce surface energy (Kothari et al. 2010; Ogolo et al. 2012). Often nanoparticles, ranging from 1 to 100 nanometers in diameters, have special optical and chemical properties at the interface, and form so-called “Pickering emulsions” (i.e., emulsions stabilized by nano or colloidal particles) (El-diasty and Aly, 2015). In addition to the fact that there is not much retention of nanoparticles in

the geological formation (because they are so small to travel a long distance through the reservoir rock (Zhang et al., 2010)), nanoparticle-stabilized emulsions have advantages over surfactant-stabilized emulsions, that is, their ability to withstand harsh conditions, being irreversibly adsorbed on the droplet surface (Fangda, 2010).

More specifically, nanoparticle emulsions have the following advantages over colloidal-particle emulsions: (i) because of smaller size, they can make emulsions more stable even at harsher conditions in terms of temperature and salinity (Mandal, 2012), (ii) they can be endowed with a certain stability and rheology by using nanoparticles manufactured with specific characteristics (for example, the magnetic, magnetostrictive, or piezoelectric characteristics of nanoparticles have been shown to control the emulsion quality, texture and de-stabilization (El-diasty and Aly, 2015), and (iii) they can be catalytic, reactive, or associative with water-soluble polymer or surfactant molecules to provide desired properties to the chemicals applied together (Melle et al., 2005; Thompson et al., 2008; El-diasty and Aly, 2015). Often, the surface properties of nanoparticles, including wettability, can be controlled by the coating materials. For example, hydrophilic nanoparticles have over 90% of silanol groups on the surface forming stable oil-in-water emulsions, while hydrophobic nanoparticles are only coated about 10% by silanol groups on their surface forming water-in-oil emulsions (Binks, 2002).

Nanoparticles form emulsions with high apparent viscosity, which helps to improve sweep efficiency from the reservoirs. Emulsion stability and rheology have been of great interest to researchers due to their dependence on electrolyte concentration and pH (Horozov et al., 2007). Theoretical models have been developed in order to understand the conditions for equilibrium and stability of emulsions stabilized with these particles, by taking electrostatic repulsions, Van der Waals attractions, and capillary attractive forces, etc. into consideration.

In spite of considerable interest shown in the previous studies, application of nanoparticles to EOR processes seems to be at its infant stage yet.

1.4 Experimental Study of Nanoparticle-stabilized Foam EOR

Experimental studies using nanoparticles for foam EOR applications are in two different categories in the literature – using nanoparticles and surfactant chemicals together, or using nanoparticles only, without surfactants. The latter fits the purpose of this study, and an example can be found from a thorough experimental study of Horjen (2015). Fig. 3 shows a schematic drawing of the experimental setup in which CO₂ foams are created by silica nanoparticles, with the total injection rates of 2, 3 and 4 cc/min (or, total velocities (u_t) of 8.46, 12.70 and 16.93 ft/day, respectively and the gas fractions (fg) between 0.1 to 1. The Bentheimer core was placed horizontally in a Hassler-type coreholder at room temperature (77 °F) and 1305 psig back-pressure. The nanoparticle concentration in the aqueous solution (2.0 wt% NaCl) was 0.5 wt%, while the CO₂ was near the supercritical state at this conditions (above the critical pressure, but slightly lower than the critical temperature). Although CO₂ at this pressure and temperature condition is a dense phase (rather than supercritical phase) strictly speaking, this study would still call it a supercritical phase because their properties are very similar.

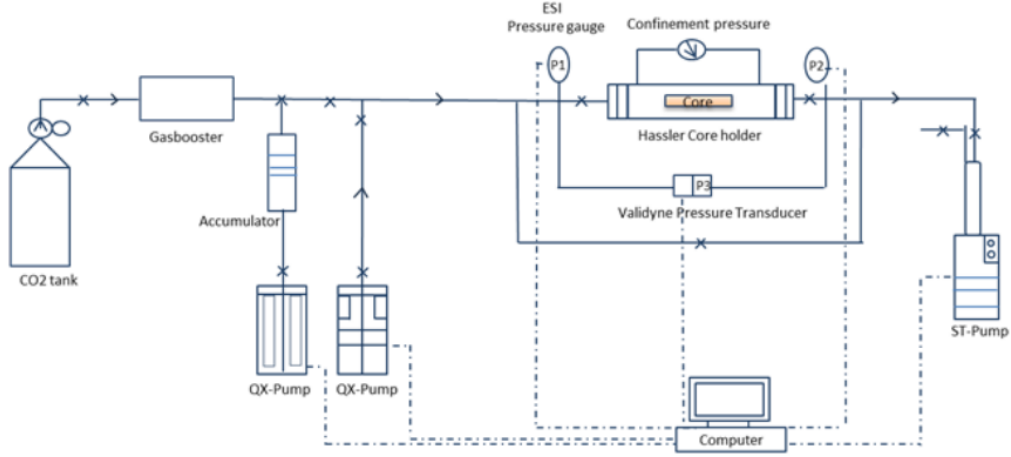


Fig. 3. Experimental setup for CO₂ foam experiments with nanoparticles at room temperature ($T = 77\text{ }^{\circ}\text{F}$). (Horjen, 2015)

Among many, a portion of the experimental results that Horjen (2015) collected by injecting CO₂ and brine simultaneously is shown in Fig. 4, which is to be used in this study for modeling purpose. This figure shows the steady-state pressure responses in a range of total injection rates and injection foam qualities (dashed lines in the absence of, and solid lines in the presence of nanoparticles (i.e., without and with foams, respectively)).

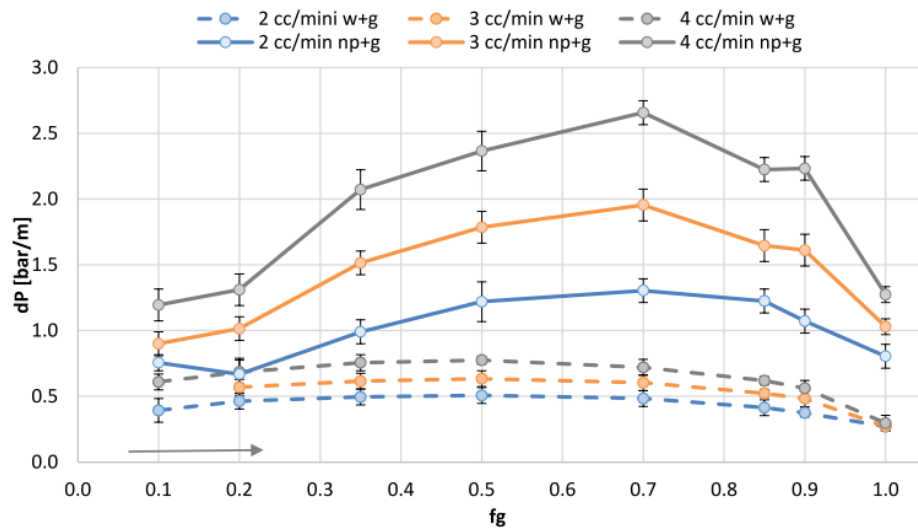
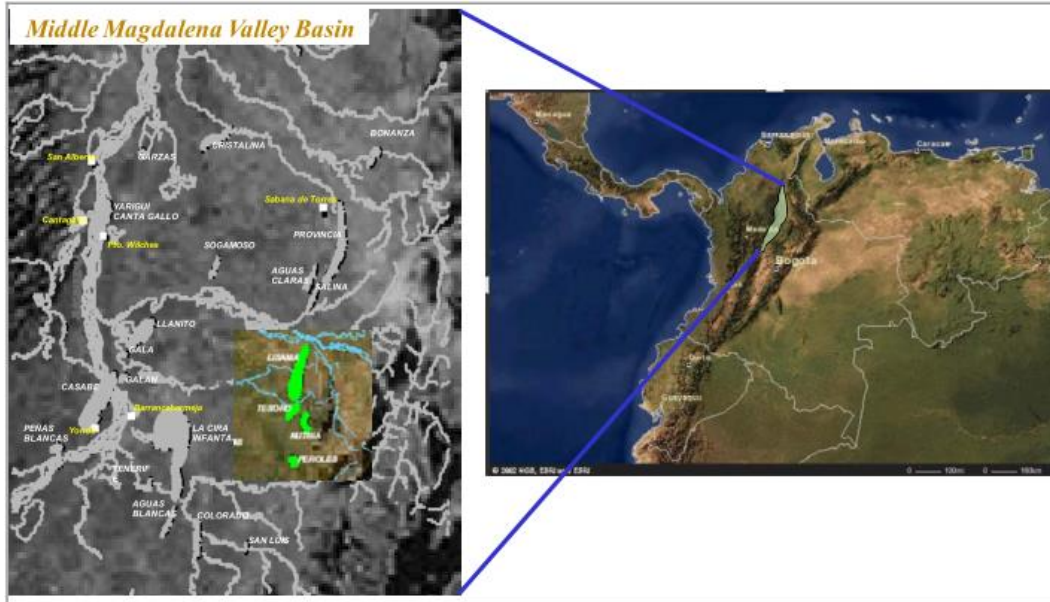


Fig. 4. Steady-state pressure-gradient (∇P) responses in a range of injection rates and injection foam qualities (no foams with dashed lines and foams with solid lines) (Horjen, 2015)

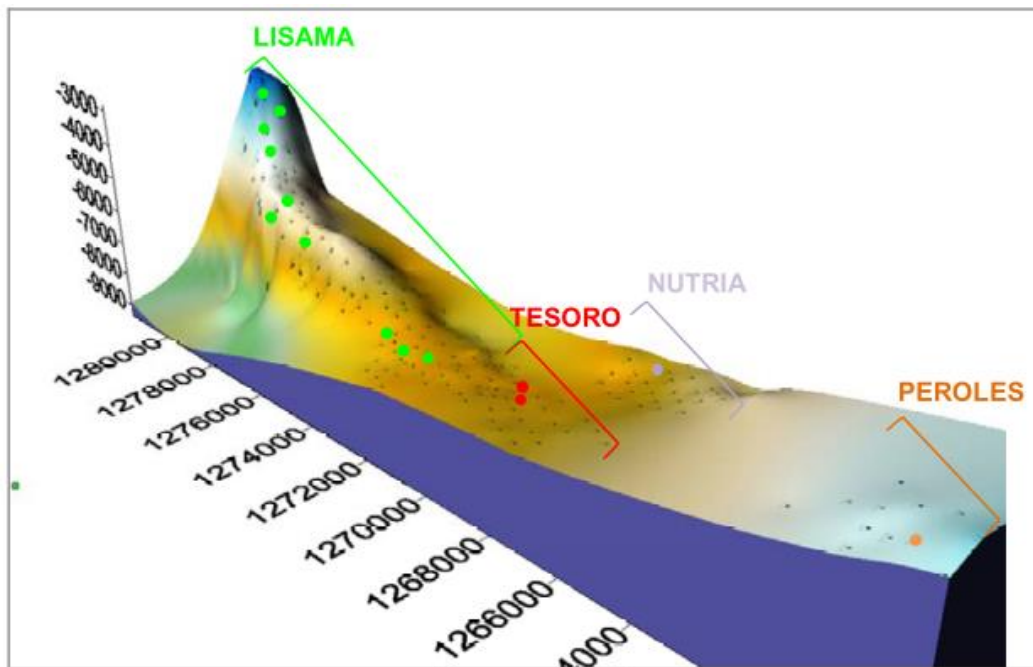
2. OBJECTIVES

The objective of this study is (i) to understand the rheological properties of nanoparticle-stabilized foams by making a model fit of mechanistic bubble-population-balance foam model to experimental data and (ii) to extend the findings into a reservoir condition similar to Lisama field in Colombia, to evaluate how much difference nanoparticle-stabilized foams can make, in contrast with conventional gas-water co-injection and surfactant-stabilized foams. The first is carried out by modifying existing mechanistic models (Kam and Rossen, 2003; Kam et al., 2007; Kam, 2008) while the second is performed with a commercial software, CMG STARS (Computer Modeling Group), with pre-specified gas mobility values.

The Lisama oilfield is located in the eastern side of the Middle Magdalena Valley Basin, as shown in Fig. 5, which has been one of the major fields in Colombia since 1939, with a cumulative oil production of 54.04 MMSTBO and a total recovery factor of about 22.48% (as of December 2011) from approximately 240 wells, slowly moving into the secondary and tertiary recovery options. More details on the field are available in Castro et al. (2009), Gomez et al. (2009), and Jaimes et al. (2014).



(a)



(b)

Fig. 5. Lisama Field to be used for simulation testing in this study: (a) location of the field in Colombia and (b) geological map showing anticline structure of the field (Castro et al., 2009)

3. METHODOLOGY

The transport equation for fluid flow in porous media is described by Darcy's equation. The Darcy's velocity (or volumetric flux) for phase j (u_j), which is simply flow rate (q_j) divided by the cross-sectional area (A , that is, $\pi D^2/4$, D being core diameter), for example, can be written as follows:

$$u_j = \frac{q_j}{A} = \frac{k k_{rj}}{\mu_j} \nabla P \quad (1)$$

where k is the absolute permeability of a medium, k_{rj} , μ_j , and $\frac{k_{rj}}{\mu_j}$ are the relative permeability, viscosity and relative mobility of phase j respectively, and ∇P (or $\Delta P/L$, L being core length in one-dimensional space) is the pressure gradient.

The use of fractional flow provides a convenient way to interpret multiphase flow in porous media. The fractional flow of water (f_w) in a conventional gas-water two-phase flow is defined as

$$f_w = \frac{u_w}{u_t} = \frac{u_w}{u_g + u_w} \quad (2)$$

where u_w is water volumetric flux, u_g is gas volumetric flux and u_t is total volumetric flux. Note that subscripts w , g , and t represent water, gas, and total (i.e., water and gas together), respectively. By combining with Darcy's equation, Eq. (2) becomes:

$$f_w = \frac{1}{1 + \frac{\mu_w k_{rg}}{k_{rw} \mu_g}} \quad (3)$$

where μ_w and μ_g are water and gas viscosities, and k_{rw} and k_{rg} are water and gas relative permeabilities, respectively. The Corey-type relative permeability functions to be applied in this study have the following forms:

$$k_{rw} = A \left[\frac{S_w - S_{wc}}{1 - S_{wc} - S_{gr}} \right]^{m_1} \quad (4)$$

$$k_{rg} = B \left[\frac{1 - S_w - S_{or}}{1 - S_{wc} - S_{gr}} \right]^{m_2} \quad (5)$$

where S_{wc} is the connate water saturation and S_{gr} is the residual gas saturation.

In order to capture bubble population balance, the rate of lamella creation R_g and the rate of lamella coalescence R_c are required. Following expressions from Kam (2008) and Afsharpoor et al. (2010):

$$R_g = \frac{C_g}{2} \left[\operatorname{erf} \left(\frac{\nabla P - \nabla P_0}{\sqrt{2}} \right) - \operatorname{erf} \left(\frac{-\nabla P_0}{\sqrt{2}} \right) \right] \quad \text{and} \quad (6)$$

$$R_c = C_c n_f \left(\frac{S_w}{S_w - S_w^*} \right)^n \quad \text{if } S_w > S_w^* \quad (7)$$

where C_g and ∇P_0 are model parameters for lamella creation, C_c and n are model parameters for lamella coalescence, ∇P , S_w , S_w^* , and n_f are the pressure gradient, water saturation, limiting water saturation, and number of lamellae per unit volume of gas, and erf is the error function. Note that the model parameter ∇P_0 is the mobilization pressure gradient that triggers a shift from weak-foam to strong-foam state (i.e., foam generation) through lamella mobilization and division in porous media. The resulting foam texture (n_f) can be determined by equating R_g and R_c , i.e.,

$$n_f = \frac{C_g}{2C_c} \left(\frac{S_w}{S_w - S_w^*} \right)^n \left[\operatorname{erf} \left(\frac{\nabla P - \nabla P_o}{\sqrt{2}} \right) - \operatorname{erf} \left(\frac{-\nabla P_o}{\sqrt{2}} \right) \right] \text{ if } n_f < n_{f \max} \quad (8)$$

The maximum foam texture ($n_{f \max}$) for strong foams in the low-quality regime corresponds roughly to the average pore size, which can be approximated by

$$n_{f \max} = \frac{1}{\frac{4}{3}\pi \left(\frac{d}{2} \right)^3} \quad (9)$$

where d is the median grain diameter of the Bentheimer sandstone core calculated using Berg's Model, i.e.,

$$d = \sqrt{\frac{k}{80.8\phi^{5.1}e^{-1.385p}}} \quad (10)$$

where, k is the absolute permeability, ϕ is the porosity in percent, and p is a sorting term, called the percentile deviation, accounting for the spread in grain size (Nelson, 1994).

The presence of foam affects the viscosity and relative permeability of gas phase significantly, but not those of liquid phase (Bernard et al., 1965; Sanchez and Schechter, 1989; Friedmann et al., 1991). To calculate gas viscosity in the presence of foam (μ_g^f), Hirasaki and Lawson (1985) suggest

$$\mu_g^f = \mu_g^o + \frac{C_f n_f}{(u_g \phi S_g X_f)^{1/3}} \quad (11)$$

where μ_g^o is gas viscosity in the absence of foam, C_f is a model parameter, ϕ is rock porosity, S_g is gas saturation and X_f is the fraction of flowing gas saturation. Therefore, Darcy's equation in the presence of foam can be written as follows:

$$u_w = \frac{k k_{rw} \nabla P}{\mu_w} \quad \text{and} \quad (12)$$

$$u_g = \frac{k k_{rg}^f \nabla P}{\mu_g^f} \quad (13)$$

where k_{rg}^f , gas relative permeability is given by

$$k_{rg}^f = k_{rg}(1 - X_t)^{m_2} \quad (14)$$

which has trapped gas saturation (X_t) defined by Kovscek et al. (1994, 1997) as follows:

$$X_t = X_{t \max} \left(\frac{\beta n_f}{1 + \beta n_f} \right) \quad (15)$$

Note that $X_{t \max}$ is the maximum fraction of trapped-gas saturation, typically ranging from 0.7 to 0.95 for stable surfactant foams, and β is the mass transfer parameter (Radke and Gillis, 1990) that defines how quickly the equilibrium state is reached.

The CMG simulation solves the governing equation that describes the isothermal, multicomponent, multiphase flow in permeable media, which is the continuity equation as follows:

$$\begin{aligned} \frac{\partial}{\partial t} (\phi \sum_{j=1}^{Np} \rho_j S_j \omega_{ij} + (1 - \phi) \rho_s \omega_{is}) + \vec{\nabla} \cdot (\sum_{j=1}^{Np} (\rho_j \omega_{ij} \vec{u}_j - \phi S_j \rho_j \vec{K}_{ij} \cdot \vec{\nabla} \omega_{ij})) = \\ \phi \sum_{j=1}^{Np} S_j r_{ij} + (1 - \phi) r_{is} \end{aligned} \quad (16)$$

where the first and second terms in the left hand side represent accumulation and convection, respectively, while the term in the right hand side represents reaction in the fluid and rock (or, sink or source term). More details on this governing equation, together with symbols, parameters and variables, are available in Lake (1989).

4. RESULTS

4.1 Model fit to small-scale lab coreflood data

The experimental data from Horjen (2015) with and without foams in Fig. 4 can be used to draw a pressure contour map as shown in Fig. 6, showing the steady-state strong-foam pressure gradient (∇P) as a function of gas velocity (u_g) and water velocity (u_w) at three different total flow rates (q_t) such as 2, 3, and 4 cc/min (or $u_t = 8.46, 12.70$, and 16.93 ft/day, equivalently). The experimental data covers foam quality (f_g) ranging 0.5 to 1, as represented by multiple straight lines coming off from the origin.

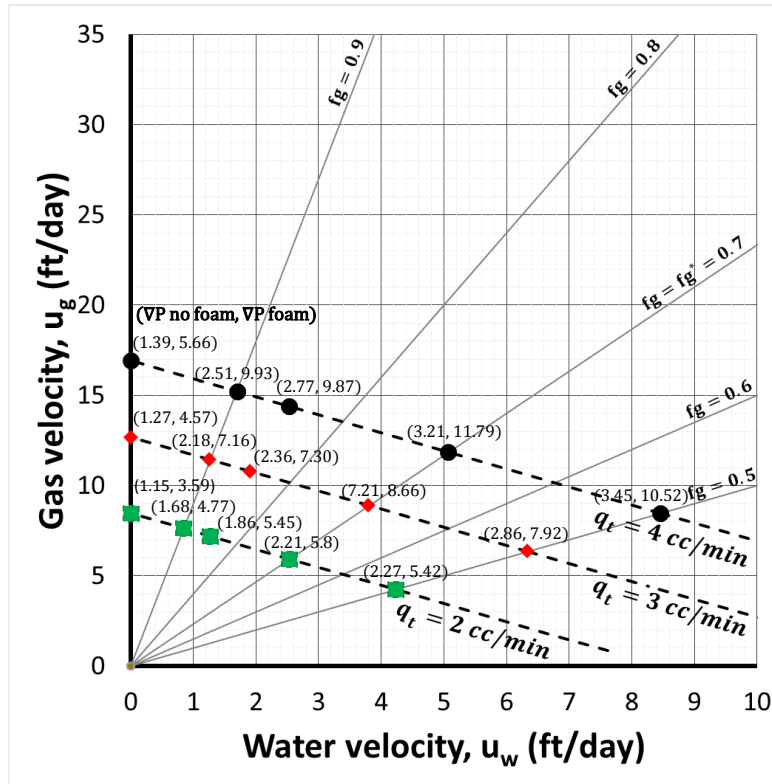


Fig. 6. Experimental data redrawn from Horjen (2015) with and without foams, showing the steady-state pressure gradient as a function of gas and liquid velocities (Note that (a, b) represents the measured pressure gradient with no foam (a) and with foam (b), both in psi/ft, respectively.) ($q_t = 2, 3$, and 4 cc/min are equivalent to $u_t = 8.46, 12.70$, and 16.93 ft/day, respectively.)

4.1.1 Construction of fractional flow curves

Because the relative permeability curves for the Bentheimer sandstone core used in Horjen (2015) are not reported, a fit to fractional flow curve with no foam offers a convenient way of determining parameters in the Corey-type relative permeability functions. Fig. 7 shows the fractional flow curve from the no-foam experimental data (see the no-foam data in Fig. 6), and Fig. 8 shows the resulting relative permeability curves for the Bentheimer Sandstone core. Note that the parameter determination (A , B , m_1 , and m_2) may not be necessarily unique, but it offers a good fit to the fractional flow curve as well as follows the general shape of relative permeability curves well for Bentheimer cores in the literature (Benson et al., 2015).

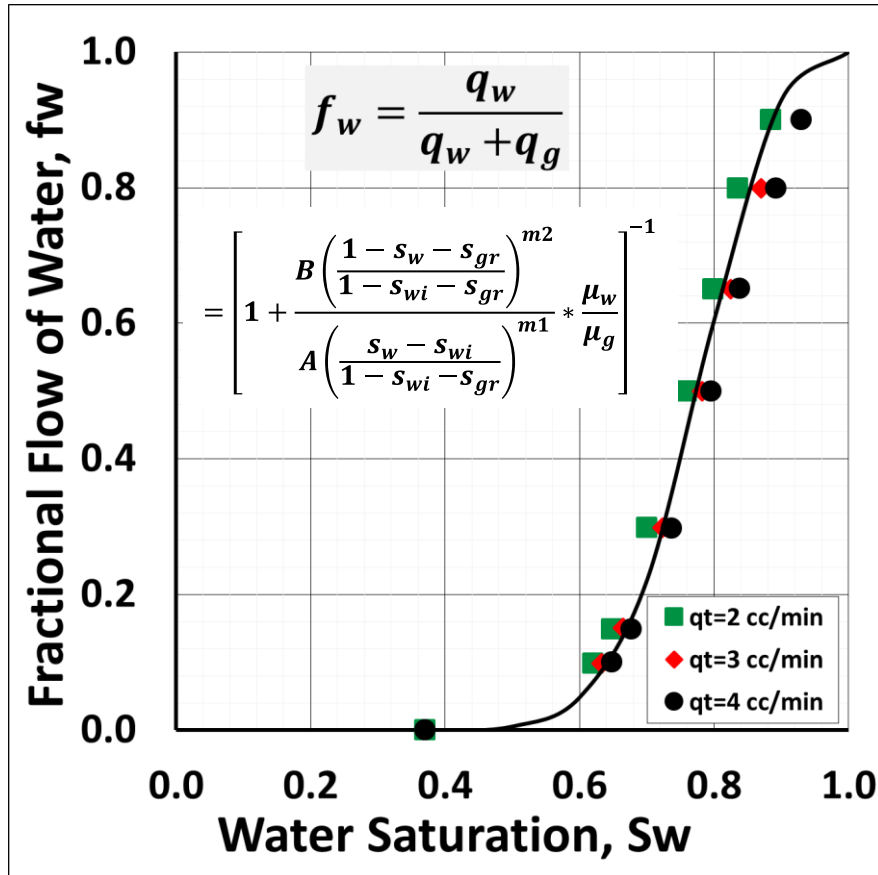


Fig. 7. Construction of fractional flow curve to estimate supercritical CO₂-brine two-phase relative permeability functions (original data from Horjen (2015) in Bentheimer cores (1305 psig and T=77 °F) at three different total injection rates (2 cc/min, 3 cc/min and 4 cc/min)

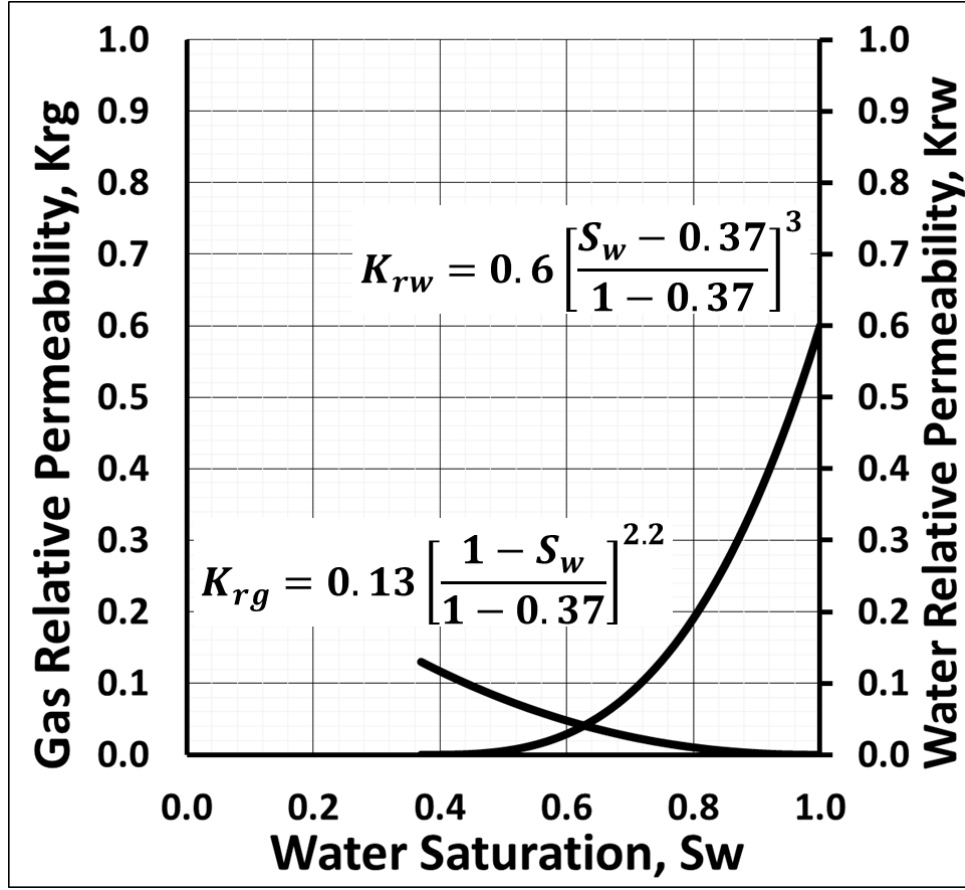


Fig. 8. Determination of CO₂-brine (no foam) relative permeability curves by making a fit to the fractional flow curve in Fig. 7 (Note that $A = 0.6$, $B = 0.13$, $m_1 = 3.0$ and $m_2 = 2.2$ when $S_{wc} = 0.37$ and $S_{gr} = 0.0$ are given)

One way to identify the level of gas-phase mobility reduction is by constructing fractional flow curves at different MRF values and comparing them with experimental data. Fig. 9 shows an example for nanoparticle-stabilized supercritical foams (with no surfactant chemicals) from Horjen (2015), and demonstrates that the range of $MRF = 3$ through $MRF = 10$ captures experimental data measured at $q_t = 2, 3$, and 4 cc/min. The curve at $MRF = 100$ can be regarded as the case when foams are created by surfactant chemicals in typical coreflood experiments. An error bar of 0.2 bar/m in Fig. 4 (dP) roughly corresponds to a change of 0.03 in water saturation in Fig. 9 (dSw).

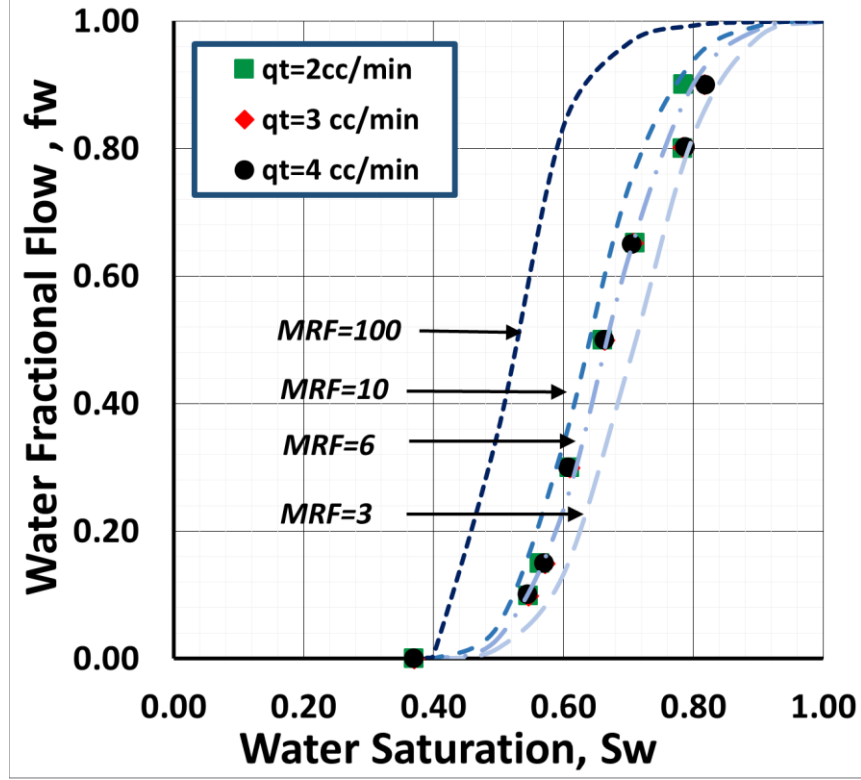


Fig. 9. Construction of fractional flow curves to fit nanoparticle-stabilized supercritical CO₂ foam experimental data (original data from Horgen (2015) in Bentheimer cores (P = 1305 psig, T = 77 °F and 0.5 wt% nanoparticles in 2 wt% NaCl brine) at three different total injection rates (2, 3 and 4 cc/min)

4.1.2 Fit of mechanistic foam model to the data

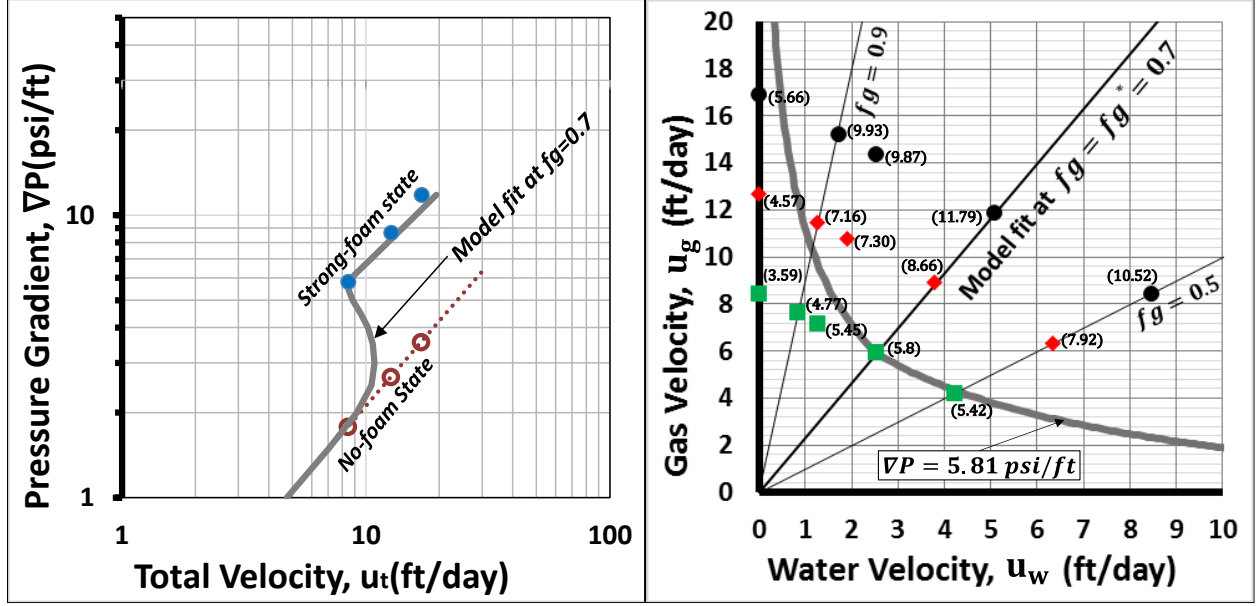
Table 1 summarizes rock properties, fluid properties and model parameters used in this study. Some rock and fluid properties are given directly from Horjen (2015), while others are estimated from the literature (for example, CO₂ viscosity from a correlation developed by Ouyang (2011), or the core's median grain diameter using Berg's Model (1970)). A “successful model fit” in this study requires a fit to at least one S-shaped curve (showing three different foam states) as well as a fit to at least one strong-foam pressure contour (showing both high-quality and low-quality regimes). Fig. 10 presents the data as an example – data points in Fig. 10(a) as an S-shape curve for no-foam and strong-foam state, showing how ∇P changes as a function of u_t at $f_g =$

0.7, and data points in Fig. 10(b) as a two flow regime map, showing the steady-state pressure gradients with the reference $\nabla P = 5.81$ psi/ft. In both plots, the solid thick lines represent a model fit by trying different combinations of mechanistic foam model parameters such as ∇P_o , C_g/C_c , C_f , n , and S_w^* , when other basic foam parameters are given (X_{tmax} , β , n_{fmax}). Note that the lower value of MRF (ranging from 3 to 10) with nanoparticle-stabilized foams (cf. Fig. 9) coincides with lower value of X_{tmax} and higher value of S_w^* .

Table 1. Summary of rock and fluid properties as well as model parameters used in this study (at 1305 psig and 77 °F).

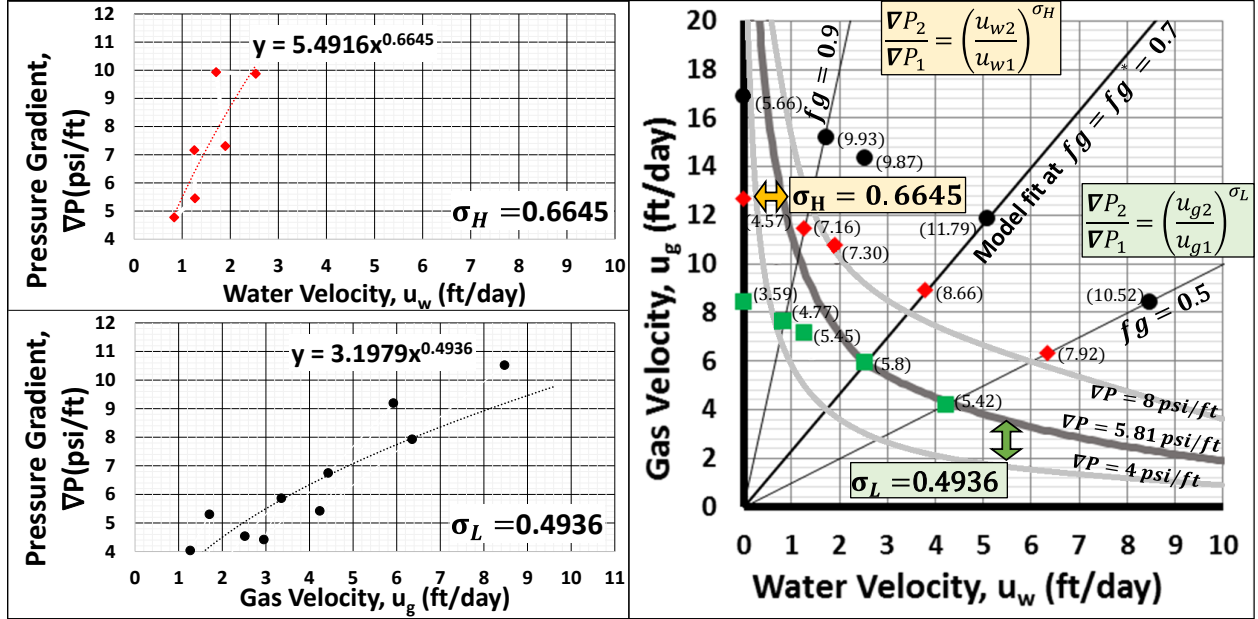
| Rock and Fluid Properties | | Model Parameters | |
|---|-------------------------------|--|--------------------------|
| | | 1. Basic Foam Parameters | |
| Core Diameter, D (inch; m) | 1.5; 0.0381 | Maximum trapped gas saturation, x_{tmax} | 0.3 |
| Core Length, L (ft; m) | 0.94; 0.286 | Gas trapping parameter, β | 5.00×10^{-11} |
| Porosity, Φ | 0.23 | Maximum foam texture, n_{fmax} | 7.88×10^{11} |
| Permeability, k (Darcy; m ²) | 2.25; 2.223×10^{-12} | Power-law exponents (high-quality regime), σ_H | 0.6645 |
| Water viscosity, μ_w (Pa·s) | 0.00108 | Power-law exponents (low-quality regime), σ_L | 0.4936 |
| | | 2. Model Fit Parameters | |
| CO ₂ viscosity, μ_g (Pa·s) | 0.00009 | Parameters for relative permeability curve (A,B,m ₁ ,m ₂) | 0.6, 0.13, 3, 2.2 |
| | | Mobilization pressure gradient, ∇P_o (psi/ft; Pa/m) | 5; 113189 |
| Connate water saturation, S_{wc} | 0.37 | Limiting water saturation, S_w^* | 0.42 |
| | | Lamella coalescence exponent, n | 1 |
| Residual gas saturation, S_{gr} | 0 | Ratio between lamella creation and coalescence parameters, C_g/C_c (1/m ³) | 3.2069×10^{12} |
| | | Foam viscosity parameter, $C_f \left(m^{7/3} \cdot kg/s^{4/3} \right)$ | 1.8271×10^{-17} |

Fig. 10(c) shows how to determine shear-thinning or shear-thickening parameters for both regimes (σ_H and σ_L in the high-quality and low-quality regimes, respectively). These parameters allow more pressure contours to be added to Fig. 10(b) to complete the map as shown in Fig. 10(d). As a result, Figs. 10(a) and 10(d) present the final outcome of the mechanistic modeling efforts.



(a)

(b)



(c)

(d)

Fig. 10. Mechanistic foam model fit to experimental data in Horgen (2015): (a) fit to three foam states ($f_g = 0.7$), (b) fit to pressure contours showing two strong-foam flow regimes ($\nabla P_{\text{ref}}=5.81$ psi/ft, $u_{w\text{ref}}=2.53$ ft/day, $u_{g\text{ref}}=5.93$ ft/day and $f_g = 0.7$), (c) shear-thinning and shear-thickening parameters determination, and (d) additional pressure contours from σ_H and σ_L in the strong-foam state. (See Table 1 for model inputs.)

As discussed earlier, the mobilization pressure gradient (∇P_o) is a key to triggering a large population of foam films in porous media, which is proportional to the ratio between gas-water interfacial tension and pore throat size (or, σ/R_t). It does not only account for CO₂ and surfactant/nanoparticle solutions (through σ), but also rock properties (through R_t , i.e., average pore size and pore size distribution). Fig. 11 shows the modeling results at three different mobilization pressure gradients ($\nabla P_o = 1, 5$ and 20 psi/ft) in terms of three foam states and two flow regimes. A lower ∇P_o is shown to stay in the strong-foam state in a wide range of velocities, which is advantageous compared to a higher level of ∇P_o (showing only a smaller range of velocity with strong foams). This implies that the design of nanoparticles that can be positioned at the CO₂ and water interface, and thus reduce interfacial tension further is a crucial component for nanoparticle-stabilized foams.

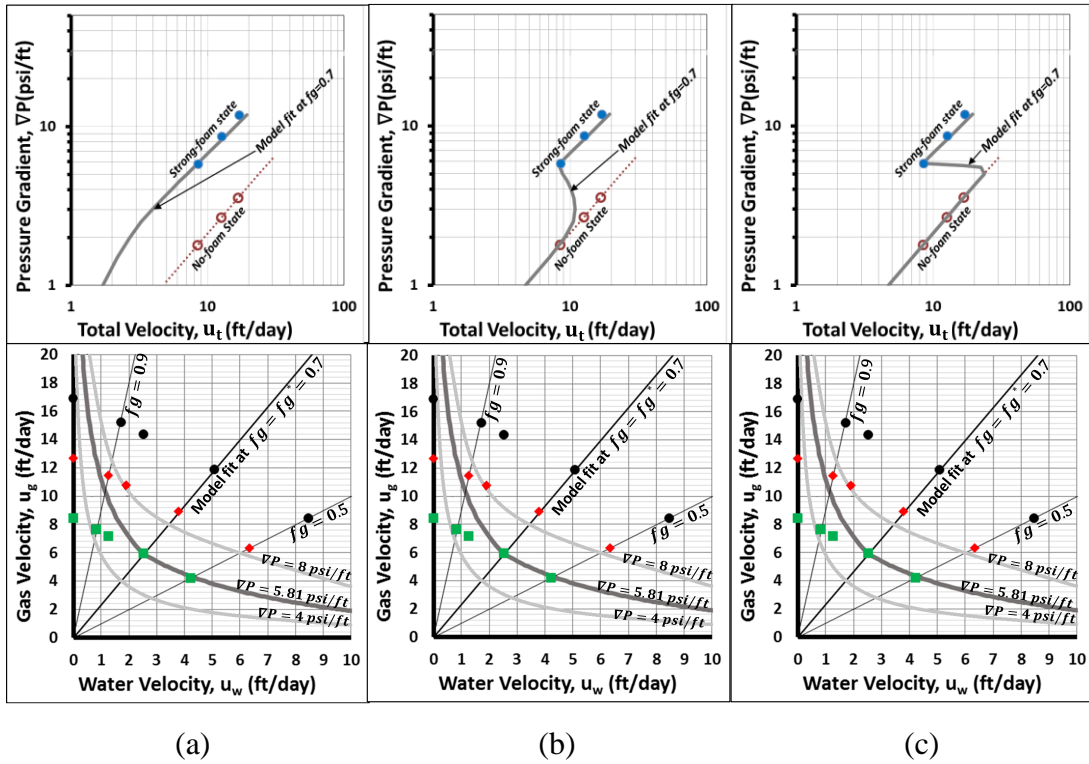


Fig. 11. Model fit to experimental data for three foam states and two strong-foam flow regimes at different mobilization pressure gradient: (a) $\nabla P_o = 1$ psi/ft, (b) $\nabla P_o = 5$ psi/ft, and (c) $\nabla P_o = 20$ psi/ft

Another important parameters are the maximum trapped gas saturation ($X_{t\max}$) and the limiting water saturation (S_w^*) because they are implicitly related to foam stability and MRF. Although better foam stability is aligned with larger $X_{t\max}$ and smaller S_w^* , their functional relationships are not easy to develop. Fig. 12(a), 12(b), and 12(c) show the modeling results at $X_{t\max}=0.1$, $S_w^* = 0.52$; $X_{t\max}=0.3$, $S_w^* = 0.42$; $X_{t\max}=0.5$, $S_w^* = 0.32$. Larger $X_{t\max}$ and smaller S_w^* makes the shift to strong-foam state at lower velocity ($u_t=9$ ft/day in Fig. 12(c) vs. $u_t=13$ ft/day in Fig. 12(a)), as expected.

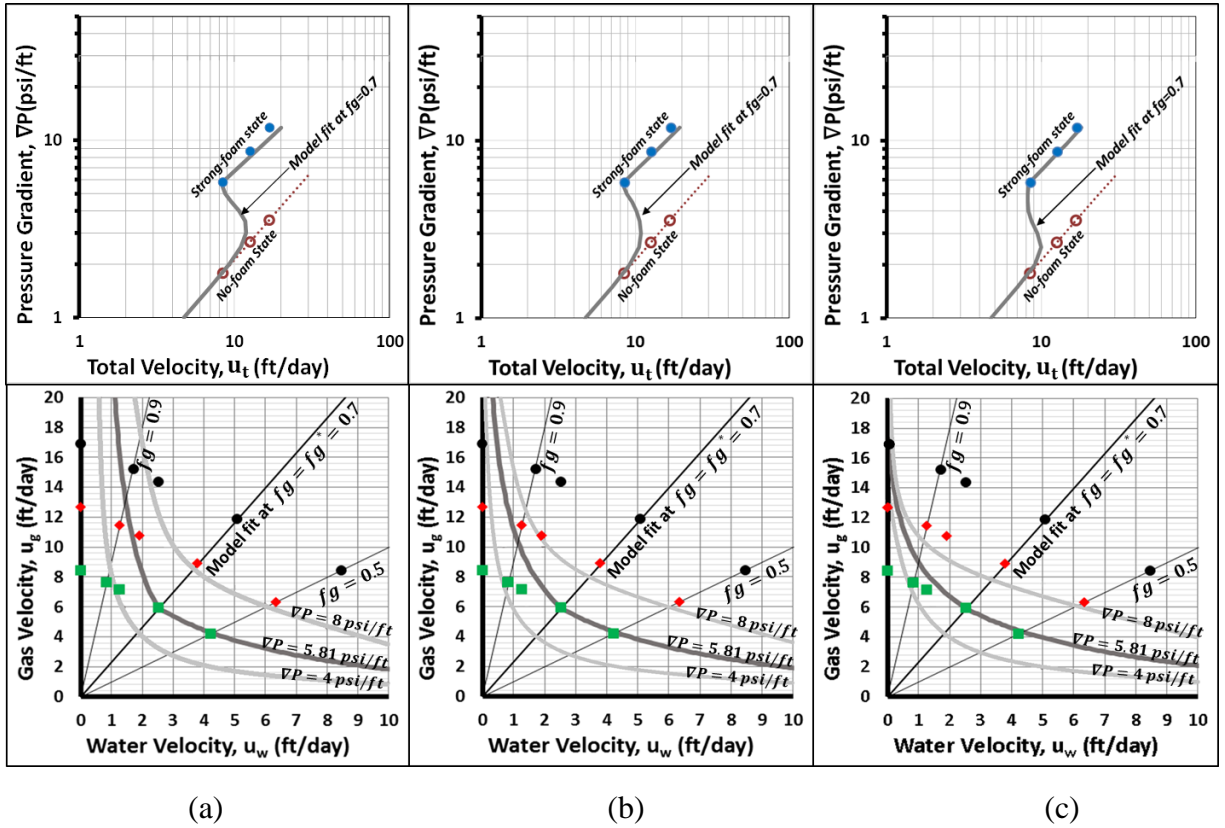


Fig. 12. Model fit to experimental data for three foam states and two strong-foam flow regimes at different maximum trapped gas saturation: (a) $X_{t\max} = 0.1$, $S_w^* = 0.52$, (b) $X_{t\max} = 0.3$, $S_w^* = 0.42$ and (c) $X_{t\max} = 0.5$, $S_w^* = 0.32$

4.1.3 Implication in displacement efficiency

In order to understand how displacement efficiency changes at different MRF values, Fig.13 constructs fractional flow curves at $MRF = 1, 3, 6, 10$ and 100 (Fig.13(a)) and the resulting saturation profiles at the dimensionless time (t_D) of 0.2 PVI (Fig.13(b)). An example graphical solution is demonstrated at $MRF = 10$: when the initial condition of the media (I) is $S_w = 1.0$ and the injection condition (J) is $f_w = 0.3$, there exists a shock wave from $S_w = 1.0$ to 0.59 governing the entire displacement process. This results in the dimensionless distance ($x_D = x/L$) of 0.38 at $t_D = 0.2$. Saturation profiles at other MRF values are also shown in Fig. 13(b) $t_D = 0.2$.

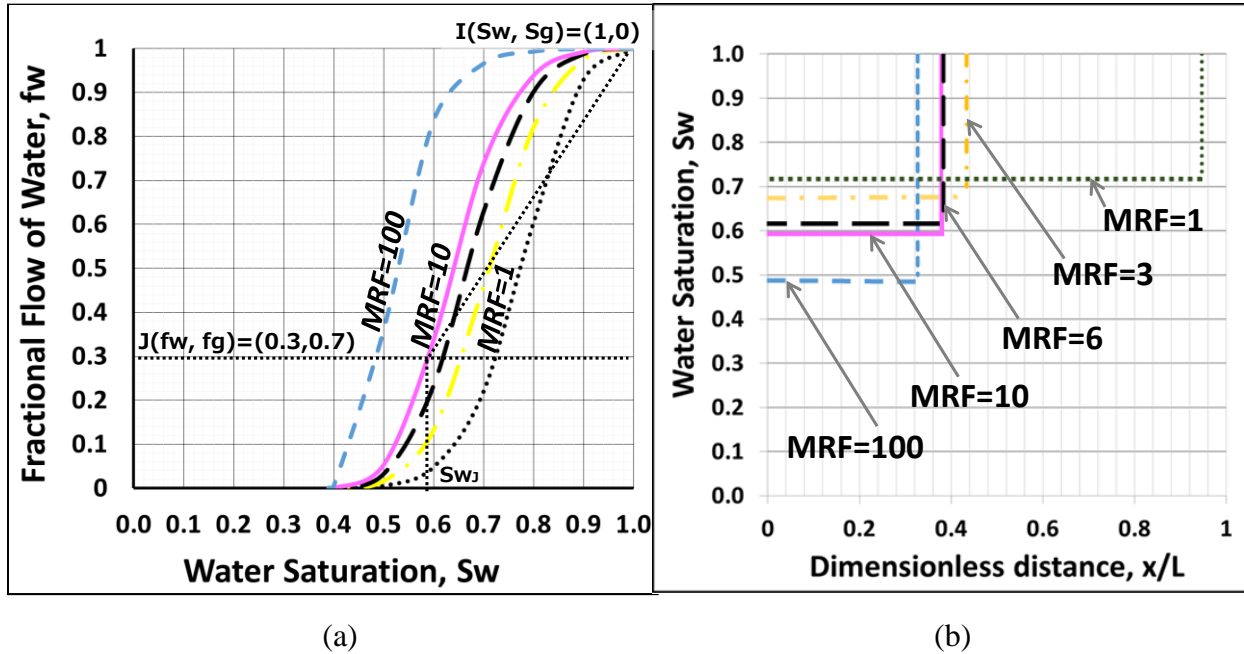


Fig. 13. Construction of fractional flow solutions in a wide range of MRF values: (a) fractional flow curves and (b) resulting saturation profiles at the dimensionless time of 0.2

Fractional flow curves can be constructed by the bubble-population-balance mechanistic foam model introduced in this study, the results of which are shown in Fig. 14(a) at $q_t = 2, 3$, and 4 cc/min. Multi-valued solutions are demonstrated within a certain range of f_w as well as S_w , as

expected, reflecting three different foam states. Corresponding changes in MRF values are shown in Fig. 14(b) (i.e., MRF vs. S_w at $q_t = 2, 3$, and 4 cc/min) and in Fig. 14(c) (i.e., f_w vs. MRF at $q_t = 2, 3$, and 4 cc/min).

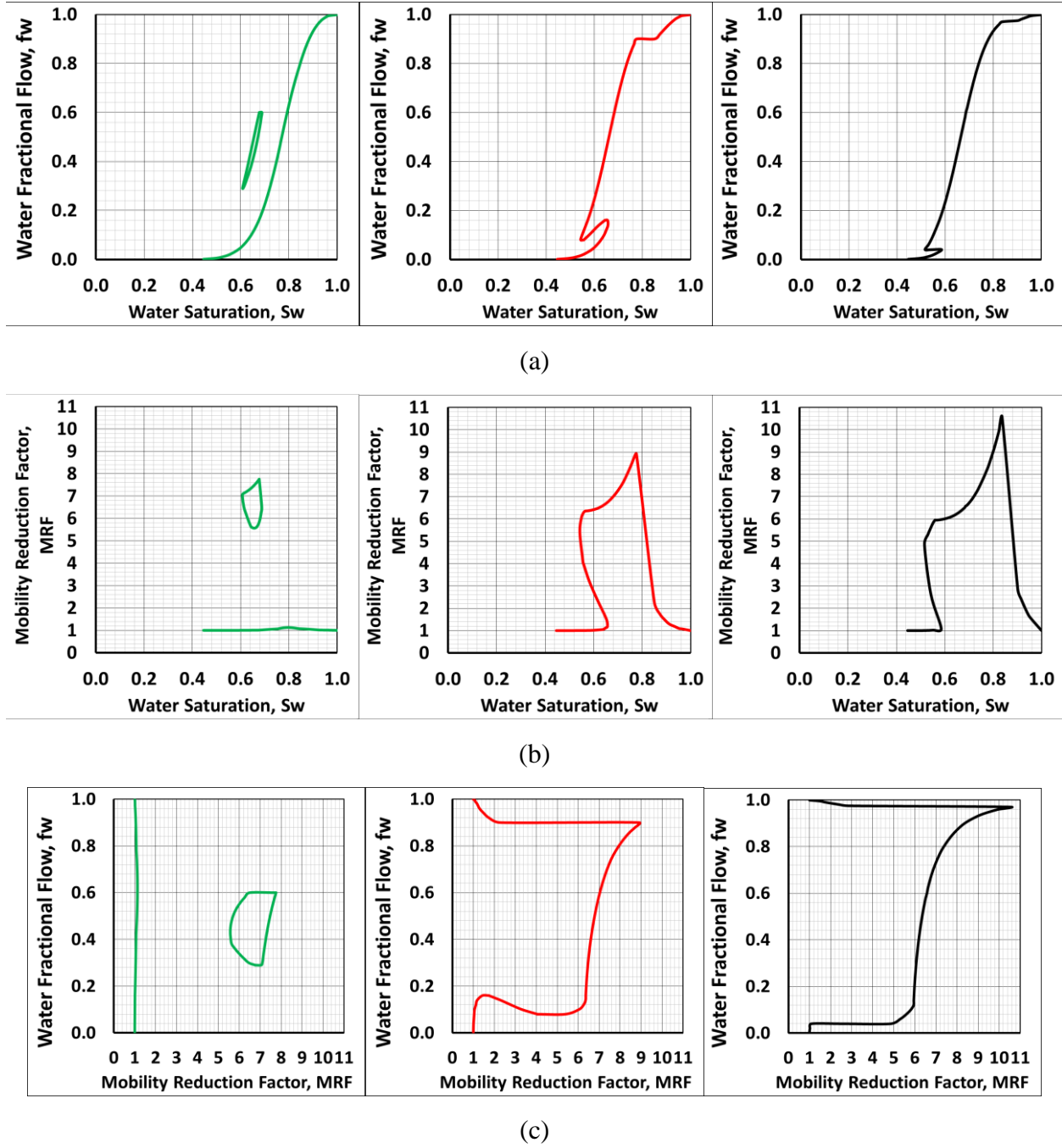


Fig. 14. Complicated fractional flow curves from bubble-population-balance mechanistic modeling: (a) fractional flow curves showing three different foam states at $q_t = 2, 3$, and 4 cc/min, (b) corresponding changes in terms of MRF vs. S_w and (c) f_w vs. MRF

4.2 Application to the field-scale treatment

Commercial reservoir simulators mostly deal with a pre-specified gas mobility reduction in simulations. This section investigates quantitatively the effect of MRF on the cumulative recovery in different scenarios from a field-scale application using CMG STARS.

4.2.1 Field description

The reservoir in Lisama Field consists of two Tertiary formations, Mugrosa and Colorado (Gomez et al., 2009), which are mainly intercalations of sandstones, mudstones and siltstones (Hammen, 1961; Morales, 1958). Lisama field has an anticline structure, and thus the hydrocarbon accumulation is related to a combination of structural and stratigraphic traps (Jaimes et al., 2014). The produced fluid is mainly black oil (32 °API), with initial bubble point pressure of 2550 psi (Sandoval et al., 2009).

This study builds a reservoir model, following Mugrosa formation characteristics, summarized in Table 2. Some input parameters were extracted from Naranjo (2010), other parameters like permeability values were assumed having as a reference the cross-section log data from Rodriguez (2009). The reservoir model has four sandstone layers intercalated with mudstones and siltstones, the top layer (A) having the highest permeability of around 100 mD, and 50, 10, and 1 mD for layers B, C, and D, respectively, from the top. This study takes the injection of gas, water, and a combination of both (with and without foams) into account with one injector and one producer (up-dip from the injector to the producer) in a vertical two-dimensional space. The injection rate or pressure is limited by the Mugrosa fracture gradient which is around 0.69 psi/ft. The grid system has a cuboidal shape with 1860 blocks in total as shown in Fig. 15.

Table 2. Simulation input for reservoir and fluid properties for CO₂, CO₂ and water, CO₂ and nanoparticle solutions, and CO₂ and surfactant solutions

| Reservoir Model and Fluid Properties | |
|--|---------|
| Original reservoir pressure (psia) @5200 ft | 2700 |
| Current reservoir pressure (psia) @5200 ft | 2500 |
| Reservoir temperature (F) | 140-160 |
| Bubble point pressure (psia) | 2500 |
| Oil viscosity (cp) @ bubble point pressure & reservoir temperature | 1.7 |
| API gravity | 28.1 |
| Oil specific gravity | 0.89 |
| Water viscosity (cp) | 0.43 |
| Initial oil saturation (%) | 75 |
| Connate water saturation (%) | 25 |
| Average porosity (%) | 0.185 |
| Fracture gradient (Psi/ft) | 0.69 |
| Permeability of layer A (mD) | 100 |
| Permeability of layer B (mD) | 50 |
| Permeability of layer C (mD) | 10 |
| Permeability of layer D (mD) | 1 |

After performing additional simulations at different grid block sizes, it is observed that a grid block size of 20 ft × 10 ft × 100 ft ($dx \times dy \times dz$ for 13 simulation scenarios in Table 4), or smaller, can capture the effect of gravity segregation reasonably well enough during water-gas coinjection, nanoparticle foam and surfactant foam displacements. A finer grid block size of 10 ft x 5 ft x 100 ft (meaning 4 times more grid blocks), in general, causes less than 0.3-0.4% change in the reported overall sweep efficiency (last column of Table 4).

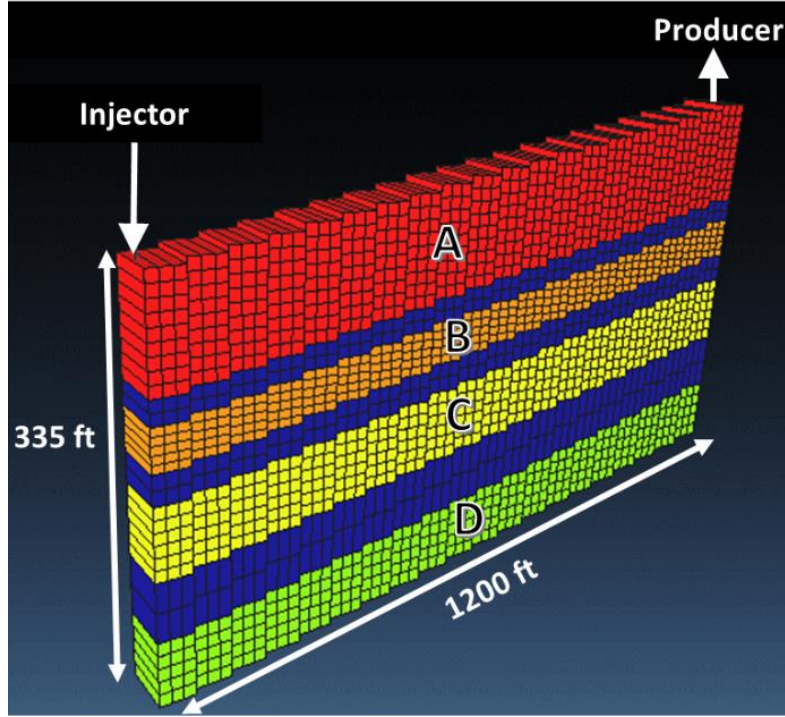


Fig. 15. Two-dimensional grid system of Mugrosa formation in Lisama Field for field-scale simulations in this study (layers A, B, C and D represent four sandstone layers isolated by impermeable layers in between)

4.2.2 Comparison of different injection scenarios

To evaluate NP CO₂ foams in field-scale applications, five main different scenarios are simulated varying mobility reduction factors, total injection rates and foam qualities as summarized in Table 3. Scenario 1 is only supercritical CO₂ injection ($f_g = 1$). The scenarios 2, 3, 4 and 5 are CO₂-water coinjection (no foams) at $f_g = 0.9$ at $q_t = 1572$ ft³/day (dry foam at low injection rate), $f_g = 0.667$ at $q_t = 1572$ ft³/day (wet foam at low injection rate), $f_g = 0.9$ at $q_t = 4379$ ft³/day (dry foam at high injection rate), and $f_g = 0.667$ at $q_t = 4379$ ft³/day (wet foam at high injection rate), respectively. The sub-scenarios 2a, 3a, 4a, and 5a use the same injection conditions, but with CO₂ and nanoparticle solutions (MRF = 10 assumed; cf. Fig. 13), while the sub-scenarios 2b, 3b, 4b and 5b use the same injection conditions, but with CO₂ and surfactant solutions (MRF = 100 assumed; cf. Fig. 13).

Table 3. Scenarios to evaluate injection of gas, gas and water (no foam), nanoparticle stabilized foams, and surfactant foams.

| Scenarios | | Gas fraction (f _g) | MRF | Water rate (bbl/day) | Water rate (ft ³ /day) | Liquid CO ₂ rate (ft ³ /day) | CO ₂ mass rate (kg/day) | Gas CO ₂ rate (SCF/day) | Total liquid rate (ft ³ /day) |
|-----------|--|--------------------------------|-----|----------------------|-----------------------------------|--|------------------------------------|------------------------------------|--|
| 1 | Supercritical CO ₂ Flooding | 100% | | 0 | 0 | 1572.1 | 32852.6 | 5.9x10 ⁵ | 1572 |
| 2 | CO ₂ -Water Coinjection | 90% | 1 | 28 | 157 | 1414.9 | 29567.3 | 5.3 x10 ⁵ | 1572 |
| 2a | CO ₂ -NP Solution Coinjection | 90% | 10 | 28 | 157 | 1414.9 | 29567.3 | 5.3 x10 ⁵ | 1572 |
| 2b | CO ₂ -Surfactant Solution Coinjection | 90% | 100 | 28 | 157 | 1414.9 | 29567.3 | 5.3 x10 ⁵ | 1572 |
| 3 | CO ₂ -Water Coinjection | 66.7% | 1 | 93 | 524 | 1048.0 | 21901.7 | 3.9 x10 ⁵ | 1572 |
| 3a | CO ₂ -NP Solution Coinjection | 66.7% | 10 | 93 | 524 | 1048.0 | 21901.7 | 3.9 x10 ⁵ | 1572 |
| 3b | CO ₂ -Surfactant Solution Coinjection | 66.7% | 100 | 93 | 524 | 1048.0 | 21901.7 | 3.9 x10 ⁵ | 1572 |
| 4 | CO ₂ -Water Coinjection | 90% | 1 | 78 | 438 | 3941.4 | 82366.1 | 1.5 x10 ⁶ | 4379 |
| 4a | CO ₂ -NP Solution Coinjection | 90% | 10 | 78 | 438 | 3941.4 | 82366.1 | 1.5 x10 ⁶ | 4379 |
| 4b | CO ₂ -Surfactant Solution Coinjection | 90% | 100 | 78 | 438 | 3941.4 | 82366.1 | 1.5 x10 ⁶ | 4379 |
| 5 | CO ₂ -Water Coinjection | 66.7% | 1 | 260 | 1460 | 2919.5 | 61012.0 | 1.1 x10 ⁶ | 4379 |
| 5a | CO ₂ -NP Solution Coinjection | 66.7% | 10 | 260 | 1460 | 2919.5 | 61012.0 | 1.1 x10 ⁶ | 4379 |
| 5b | CO ₂ -Surfactant Solution Coinjection | 66.7% | 100 | 260 | 1460 | 2919.5 | 61012.0 | 1.1 x10 ⁶ | 4379 |

Table 4 shows a summary of simulations following the scenarios, showing the cumulative oil production, remaining oil saturation, and sweep efficiency after 9 years of injection (note that the oil saturation at the beginning of injection is 0.75). The results show that (i) in all cases NP CO₂ foams perform better than CO₂-water injection (no foam), but not as efficient as surfactant foams; (ii) although NP CO₂ foams enhance oil recovery, the increment oil production is not as

impressive as hoped for; and (iii) this implies that how to engineer nanoparticles to make gas mobility further reduced and thus sweep efficient improved still remains as a future challenge.

Table 4. Summary of the results from 13 different 9-year injection scenarios (also see Table 3) in terms of cumulative oil recovery, remaining oil saturation and sweep efficiency

| Scenarios | | Gas fraction (f _g) | MRF | Total liquid Rate (ft ³ /day) | Cumulative oil production (Mbbl) | Remaining oil saturation (%) | Sweep efficiency (%) |
|-----------|--|--------------------------------|-----|--|----------------------------------|------------------------------|----------------------|
| 1 | Supercritical CO ₂ Flooding | 100% | | 1572 | 42 | 71% | 5% |
| 2 | CO ₂ -Water Coinjection | 90% | 1 | 1572 | 93 | 66% | 12% |
| 2a | CO ₂ -NP Solution Coinjection | 90% | 10 | 1572 | 98 | 65% | 13% |
| 2b | CO ₂ -Surfactant Solution Coinjection | 90% | 100 | 1572 | 110 | 64% | 14% |
| 3 | CO ₂ -Water Coinjection | 66.7% | 1 | 1572 | 216 | 53% | 29% |
| 3a | CO ₂ -NP Solution Coinjection | 66.7% | 10 | 1572 | 220 | 53% | 29% |
| 3b | CO ₂ -Surfactant Solution Coinjection | 66.7% | 100 | 1572 | 235 | 51% | 31% |
| 4 | CO ₂ -Water Coinjection | 90% | 1 | 4379 | 204 | 55% | 27% |
| 4a | CO ₂ -NP Solution Coinjection | 90% | 10 | 4379 | 215 | 53% | 29% |
| 4b | CO ₂ -Surfactant Solution Coinjection | 90% | 100 | 4379 | 256 | 49% | 34% |
| 5 | CO ₂ -Water Coinjection | 66.7% | 1 | 4379 | 273 | 47% | 37% |
| 5a | CO ₂ -NP Solution Coinjection | 66.7% | 10 | 4379 | 278 | 47% | 38% |
| 5b | CO ₂ -Surfactant Solution Coinjection | 66.7% | 100 | 4379 | 303 | 44% | 41% |

The Appendix section has detailed simulation results in terms of production rate and cumulative recovery for 9 years of injection (Figs. A.1 through A.13) as well as remaining oil saturation at the end of 9 years injection (Figs. A.14 through A.18) for all 13 scenarios.

5. CONCLUSIONS AND RECOMMENDATIONS

- This study shows how a mechanistic bubble-population-balance foam model successfully reproduces coreflood experimental data (Horjen, 2015) for nanoparticle-stabilized supercritical CO₂ foams by creating three foam states (weak-foam, strong-foam, and intermediate states) and two steady-state strong-foam regimes (high-quality and low-quality regimes).
- This study also shows how to make a fit to the experimental data, when there is an uncertainty in estimating the mobilization pressure gradient and foam stability, through ∇P_o , $X_{t\max}$, and S_w^* . They are affected by surfactant chemistry and rock and fluid properties. When the result of mechanistic foam model is compared with a local-equilibrium foam model, nanoparticle-stabilized supercritical CO₂ foams exhibit the gas-phase mobility reduction by up to about 10 (MRF ~ 10). This value is much lower than a typical value observed with surfactant foams (MRF~100 range) in lab core flooding experiments.
- When field-scale simulations are performed with CMG for the cross-section between one injection well and one production well, the results show that although nanoparticle-stabilized CO₂ foam is advantageous over the conventional gas-liquid co-injection (no foam), the sweep efficiency is lower than that of surfactant CO₂ foam.
- The use of nanoparticle technology has emerged due to nanoparticle's high stability at severe reservoir conditions and ability to control desorption and degradation of surfactant molecules. However, more in-depth research is needed to enhance nanoparticle properties (including surface coating as well as particle itself) for improved stability and strength of nanoparticle-stabilized foams.

- The process of simultaneous injection of water and supercritical CO₂ without foam shows an increase in sweep efficiency by up to 32%, when compared to supercritical CO₂ gas-only flooding. It is because the injected water can sweep the oil in the lower part of the reservoir that cannot be easily accessible by CO₂. A relatively lower amount of additional oil recovery by using either nanoparticle and surfactant foams is somewhat unexpected, but the result is highly field-specific obviously.

REFERENCES

- Afsharpoor, A., Lee, G. S., Kam, S. I., 2010. Mechanistic Simulation of Continuous Gas injection Period during Surfactant-Alternating-Gas (SAG) Processes Using Foam Catastrophe Theory. *Chemical Engineering Science*, 65(11), 3615-3631.
- Alvarez, J. M., Rivas, H. J., Rossen, W. R., 2001. Unified Model for Steady-State Foam Behavior at High and Low Foam Qualities. *SPE J.* 6 (3): 325–333. SPE-74141-PA. <http://dx.doi.org/10.2118/74141-PA>.
- Benson, S. M., Hingerl, F., Zuo, L., Pini, R., Krevor, S., Reynolds, C., ... Niemi, A., 2015. Relative permeability for multi-phase flow in CO₂ storage reservoirs. Part II: resolving fundamental issues and filling data gaps. Global CCS Institute.
- Berg, R., 1970. Method for determining permeability from reservoir rock properties. *Transaction: Gulf Coastal Association of Geological Societies*, v.XX, P.303-317.
- Bernard, G. G., Jacobs, W.L., 1965. Effect of Foam on Trapped Gas Saturation and on Permeability of Porous Media to Water. *Society of Petroleum Engineers Journal*, 5(4): 295–300.
- Binks, B. P., 2002. Particles as surfactants—similarities and differences. *Current Opinion in Colloid & Interface Science*, 7(1–2): 21-41.
- Castro, R., Sandoval, J. R., Soto, C., Pérez, H., Sandoval, J., Trujillo, M.,... Rodriguez, E., 2009. New Approach to Integrate Reservoir and Geological Information in Complex Fluvial-Stratigraphic Environments to Determine Potential Areas for Water Injection Processes. *SPE* 122108.
- Dholkawala, Z. F., Sarma, H. K., Kam, S. I., 2007. Application of fractional flow theory to foams in porous media. *Journal of Petroleum Science and Engineering*, 57(1–2), 152–165. <https://doi.org/10.1016/j.petrol.2005.10.012>

- El-diasty, A. I., Aly, A. M., 2015. Understanding the Mechanism of Nanoparticles Applications in Enhanced Oil Recovery. In SPE North Africa Technical Conference and Exhibition (Vol. 0, pp. 1–19). Cairo: SPE.
- Fangda Q., Daulat M., 2010. Experimental Study of Solvent-Based Emulsion Injection to Enhance Heavy Oil Recovery in Alaska North Slope Area. CSUG/SPE 136758, DOI: 10.2118/136758-MS
- Ferno, M. A., Gauteplass, J., Pancharoen, M., Haugen, A., Graue, A., Kovscek, A. R., and Hirasaki, G., 2014. Experimental Study of Foam Generation, Sweep Efficiency and Flow in a Fracture Network. Society of Petroleum Engineers.
- Friedmann, F., Chen, W.H., Gauglitz, P.A., 1991. Experimental and simulation study of high-temperature foam displacement in porous media. SPERE 37–45 (February).
- Gauglitz, P.A., Friedmann, F., Kam, S.I., Rossen, W.R., 2002. Foam generation in homogeneous porous media. Chem. Eng. Sci. 57, 4037–4052.
- Gomez Moncada, R. A., Morales Rojas, J., Perez Vega, H. H., Sandoval Munoz, J. E. E., Bohorquez, M. A. J., 2009. Impact Analysis and Interpretation of the Sand Thickness Obtained From Electric Logs and Outcrops in the Geostatistical Modeling of Stratigraphic Complex. Society of Petroleum Engineers. doi:10.2118/122234-MS
- Grundmann, S., Lord, D., 1983. Foam Stimulation. Journal of Petroleum Technology, 35(3), 597–602. <https://doi.org/10.2118/9754-PA>
- Hammen, V., 1961. Lexico Estratigráfico. INGEOMINAS
- Hanssen, J. E., M. Dalland., 1990. Foams for Effective Gas Blockage in the Presence of Crude Oil, Society of Petroleum Engineers.
- Hirasaki, G. J., 1989. The Steam-Foam Process. Society of Petroleum Engineers. doi:10.2118/19505-PA

- Hirasaki, G. J., Lawson, J. B., 1985. Mechanisms of Foam Flow in Porous Media: Apparent Viscosity in Smooth Capillaries. SPE J. 25 (2): 176–190. SPE-12129-PA. <http://dx.doi.org/10.2118/12129-PA>
- Horjen, H. T., 2015. CO₂ Foam Stabilization with Nanoparticles and EOR in Fractured Carbonate Systems. MA thesis, University of Bergen, Norway.
- Horozov, T. S., Binks, B. P., Gottschalk-Gaudig, T., 2007. Effect of Electrolyte in Silicone Oil-in-Water Emulsions Stabilized by Fumed Silica Particles. Phys. Chem. Chem. Phys., 9, 6389–6404.
- Jaimes, M. G., Quintero, Y. A., Contreras, G. Y., 2014. Drawdown Management: A Technical and Economic Alternative for Sand Control in Wells: A Colombian Field Application. Society of Petroleum Engineers. doi:10.2118/169376-MS
- Kam, S. I., 2008. Improved Mechanistic Foam Simulation with Foam Catastrophe Theory. Colloids and Surfaces A: Physicochemical and Engineering Aspects, (318(1), 62-77).
- Kam, S. I., Rossen, W. R., 2002. A Model for Foam Generation in Homogeneous Media. Society of Petroleum Engineers. doi:10.2118/77698-MS
- Kam, S. I., Rossen, W. R., 2003. A Model for Foam Generation in Homogeneous Porous Media. SPE Journal , 417-425 (December).
- Kam, S., Nguyen, Q., Li, Q., Rossen, W., 2007. Dynamic Simulations With an Improved Model for Foam Generation. SPE Journal, 12(April 2006), 26–29. <https://doi.org/10.2118/90938-PA>
- Kang, P.-S., Lim, J.-S., Huh, C., 2014. Screening Criteria for Application of EOR Processes in Offshore Fields. 24th International Ocean and Polar Engineering Conference, 3, 159–165.
- Khatib, Z. I., Hirasaki, G. J., Falls, A. H., 1988. Effects of Capillary Pressure on Coalescence and Phase Mobilities in Foams Flowing Through Porous Media. SPE Reservoir Engineering, 3(3), 919–926. <https://doi.org/10.2118/15442-PA>

Kothari, N., Raina B., Chandak, K., Iyer V., Mahajan, H., 2010. Application of Ferrofluid for Enhanced Surfactant Flooding in EOR, SPE Europe/Eage Annual Conference and Exhibition, 14 – 17 June 2010, Barcelona, Spain, Paper No. 131272 – MS, Pp. 1 – 7.

Kovscek, A. R., Patzek, T. W., Radke, C. J., 1997. Mechanistic Foam Flow Simulation in Heterogeneous and Multidimensional Porous Media. SPE J. 2 (4). SPE-39102-PA. <http://dx.doi.org/10.2118/39102-PA>

Kovscek, A.R., Radke, C.J., 1994. Fundamentals of Foam Transport in Porous Media. In Foams: Fundamentals and Applications in the Petroleum Industry. L.L. Schramm (ed.). ACS Advances in Chemistry Series No. 242. Washington, DC: Am. Chem. Soc.

Lake, L.W. 1989., Enhanced Oil Recovery. Englewood Cliffs, New Jersey: Prentice Hall.

Mandal, A., Bera, A., Ojha, K., Kumar, T., 2012. Characterization of Surfactant Stabilized Nanoemulsion and Its Use in Enhanced Oil Recovery. SPE 155406, DOI: 10.2118/ 155406-MS

Manrique, E., Thomas, C., Ravikiran, R., Izadi, M., Lantz, M., Romero, J., Alvarado, V., 2010. EOR: current status and opportunities. Society of Petroleum Engineers, 1–21. <https://doi.org/10.2118/130113-MS>

Melle, S., Lask, M., Fuller, G. G., 2005. Pickering Emulsions with Controllable Stability, Langmuir, 21, 2158-2162.

Morales, V., 1958. Lexico Estratigráfico. INGEOMINAS

Naranjo, C., 2010. Factibilidad de La Inyeccion de Agua en las Arenas Mugrosa del Campo Lisama. Universidad Industrial de Santander, Bucaramanga.

Nelson, P. H., 1994. Permeability-porosity Relationships In Sedimentary Rocks. Society of Petrophysicists and Well-Log Analysts.

- Ogolo, N. C., Olafuyi, O. A., Onyekonwu, M., 2012. Enhanced Oil Recovery Using Nanoparticles. Saudi Arabia Section Technical Symposium and Exhibition, 9. <https://doi.org/10.2118/160847-MS>
- Osterloh, W. T., Jante, M. J., 1992. Effects of Gas and Liquid Velocity on Steady-State Foam Flow at High Temperature. Society of Petroleum Engineers, 237–248. <https://doi.org/10.1143/JJAP.37.925>
- Ouyang, L.B., 2011. New Correlations for Predicting the Density and Viscosity of Supercritical Carbon Dioxide Under Conditions Expected in Carbon Capture and Sequestration Operations. The Open Petroleum Engineering Journal, 4, 13–21.
- Radke, C. J., Gillis, J. V., 1990. A Dual Gas Tracer Technique for Determining Trapped Gas Saturation During Steady Foam Flow in Porous Media. Society of Petroleum Engineers. Retrieved from <https://www-onepetro-org.libezp.lib.lsu.edu/download/conference-paper/SPE-20519-MS?id=conference-paper%2FSPE-20519-MS>
- Ransohoff, T. C., Radke, C. J., 1988. Mechanisms of Foam Generation in Glass-Bead Packs. SPE Reservoir Engineering, 3(2), 573–585. <https://doi.org/10.2118/15441-PA>
- Rossen, W. R., Bruining, J., 2007. Foam Displacements with Multiple Steady States. SPE Journal, 12(1), 5–18. <https://doi.org/10.2118/89397-PA>
- Rodriguez, P., 2009. Evaluacion Tecnica de la Implementacion de un Proceso de Inyeccion de Agua en el Campo Lisama Mediante Simulacion Numerica de Yacimientos. Universidad Industrial de Santander, Bucaramanga.
- Sanchez, J.M., Schechter, R. S., 1989, Surfactant effects on the two-phase flow of steam-water and nitrogen-water through permeable media. Journal of Petroleum Science and Engineering, 3(1-2): 185–199
- Sandoval, J. R., Sandoval, J., Soto, C. P., Perez, H. H., Trujillo Portillo, M. L., Cardenas, F. A., ... Rodriguez, E., 2009. New Approach to Integrate Reservoir and Geological Information in Complex Fluvial-Stratigraphic Environments to Determine Potential Areas for Water Injection Processes. Society of Petroleum Engineers. doi:10.2118/122108-MS

Sandrea, R., 2016. Approach screens reservoir candidates for EOR. Oil & Gas Journal, April 18.

Schramm, L. L., 1994. Foams: Fundamentals and applications in the petroleum industry. Petroleum Recovery Institute, American Chemical Society (Vol. 36). [https://doi.org/10.1016/0140-6701\(95\)95394-9](https://doi.org/10.1016/0140-6701(95)95394-9)

Skoreyko, F., Pino, A. V., Prada, H. R., Nguyen, Q. P., 2011. Development of a New Foam EOR Model From Laboratory and Field Data of the Naturally Fractured Cantarell Field. SPE Reservoir Characterisation and Simulation Conference and Exhibition, (1999), 1–15. <https://doi.org/10.2118/145718-MS>

Thompson, J., Vasquez, A., Hill, J. M., Pereira-Almao, P., 2008. The Synthesis and Evaluation of Up-scalable Molybdenum based Ultra Dispersed Catalysts: Effect of Temperature on Particle Size. Catal. Lett., 123, 16-23.

U.S. Energy Information Administration. 2016. International Energy Outlook 2016. International Energy Outlook 2016 (Vol. 0484(2016)). [https://doi.org/www.eia.gov/forecasts/ieo/pdf/0484\(2016\).pdf](https://doi.org/www.eia.gov/forecasts/ieo/pdf/0484(2016).pdf)

Zhang, T., Davidson, D., Bryant, S., Huh, C., 2010. Nanoparticle-Stabilized Emulsions for Applications in Enhanced Oil Recovery. Proceedings of SPE Improved Oil Recovery Symposium. <https://doi.org/10.2118/129885-MS>

APPENDIX A

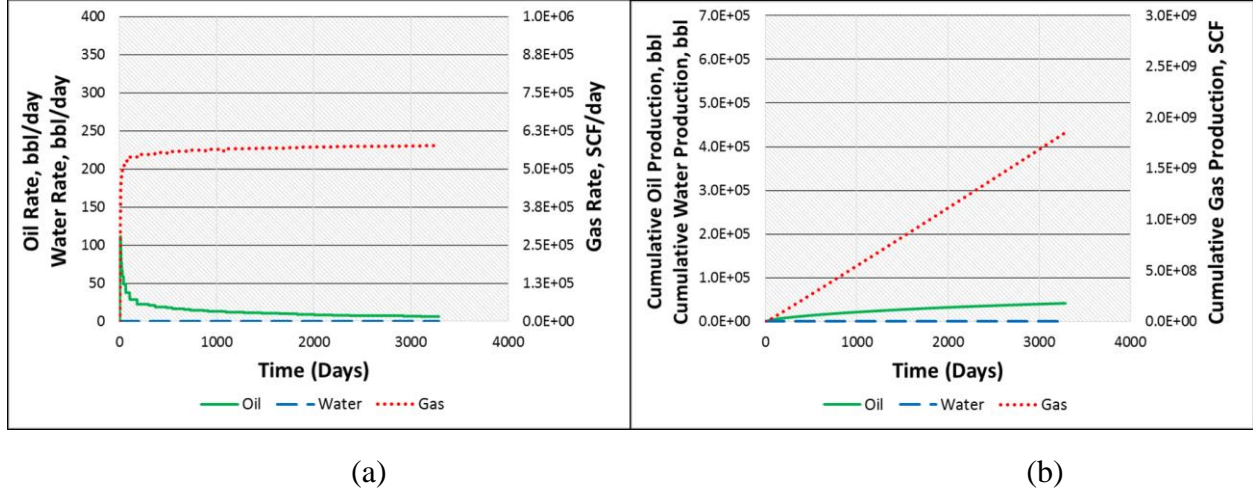


Fig. A1. Evaluation of supercritical CO₂ flooding, scenario 1 in Table 3, with $f_g = 1$ and $q_t = 1572$ ft³/day at reservoir condition): (a) production rates and (b) cumulative production (9 years)

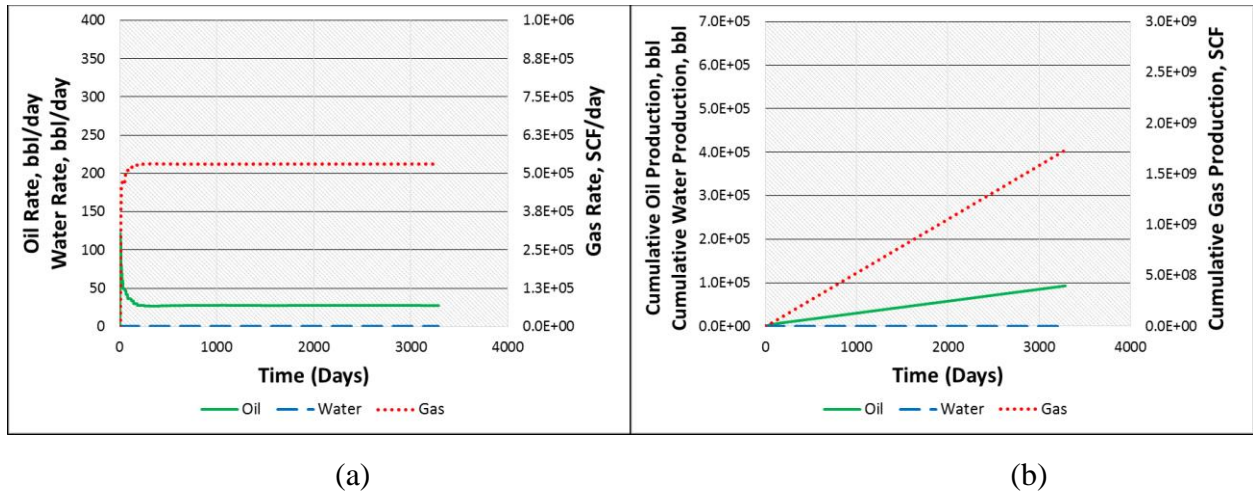
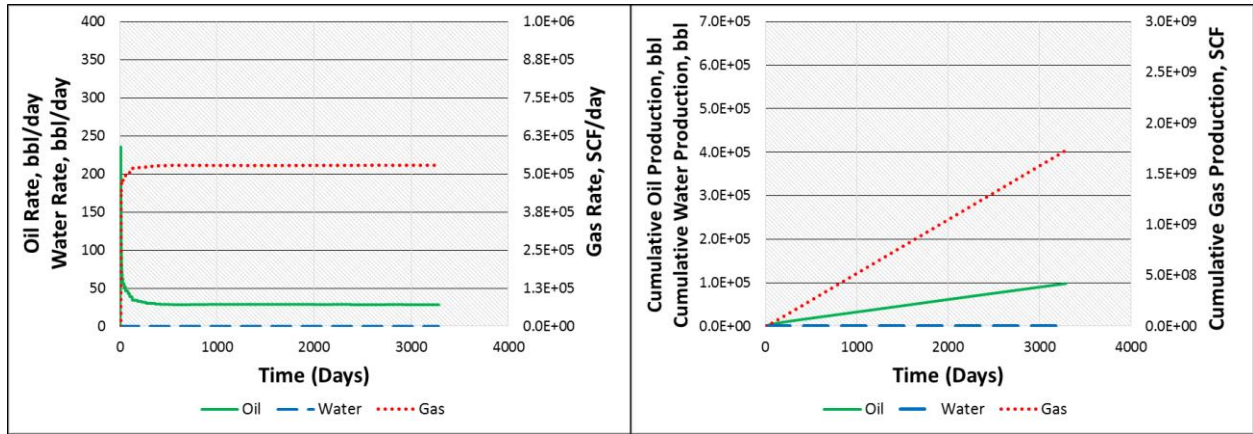


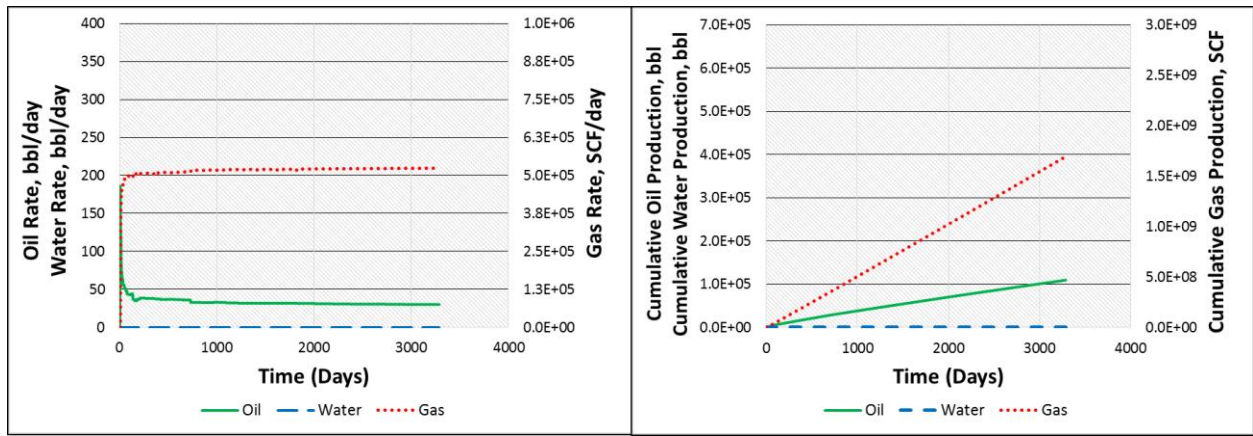
Fig. A2. Evaluation of supercritical CO₂ and water co-injection (MRF = 1 (no foam); scenario 2 in Table 3 with $f_g = 0.90$ and $q_t = 1572$ ft³/day at reservoir condition): (a) production rates and (b) cumulative production (9 years)



(a)

(b)

Fig. A3. Evaluation of supercritical CO₂ and nanoparticle solution co-injection (MRF = 10; scenario 2a in Table 3 with $f_g=0.90$ and $q_t=1572$ ft³/day at reservoir condition): (a) production rates and (b) cumulative production (9 years)



(a)

(b)

Fig. A4. Evaluation of supercritical CO₂ and surfactant solution co-injection (MRF = 100; scenario 2b in Table 3 with $f_g=0.90$ and $q_t=1572$ ft³/day at reservoir condition): (a) production rates and (b) cumulative production (9 years)

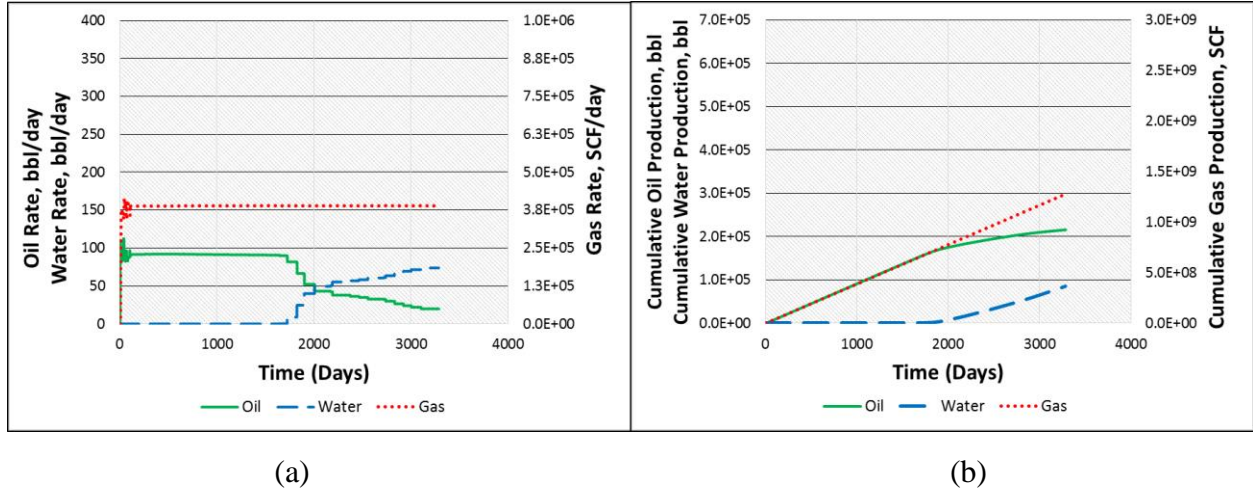


Fig. A5. Evaluation of supercritical CO₂ and water co-injection (MRF = 1 (no foam); scenario 3 in Table 3 with $f_g = 0.66$ and $q_t = 1572 \text{ ft}^3/\text{day}$ at reservoir condition): (a) production rates and (b) cumulative production (9 years)

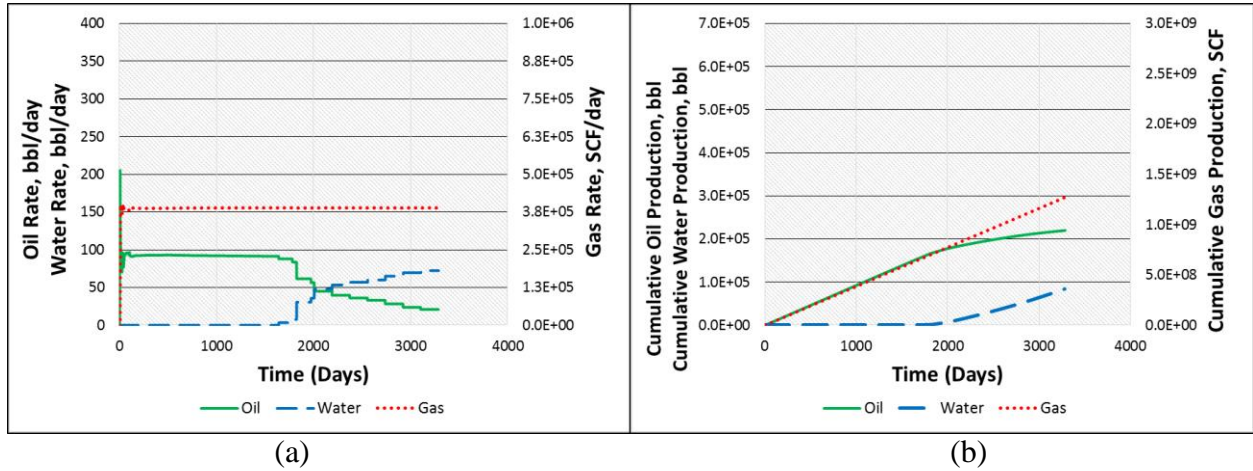


Fig. A6. Evaluation of supercritical CO₂ and nanoparticle solution co-injection (MRF = 10; scenario 3a in Table 3 with $f_g = 0.66$ and $q_t = 1572 \text{ ft}^3/\text{day}$ at reservoir condition): (a) production rates and (b) cumulative production (9 years)

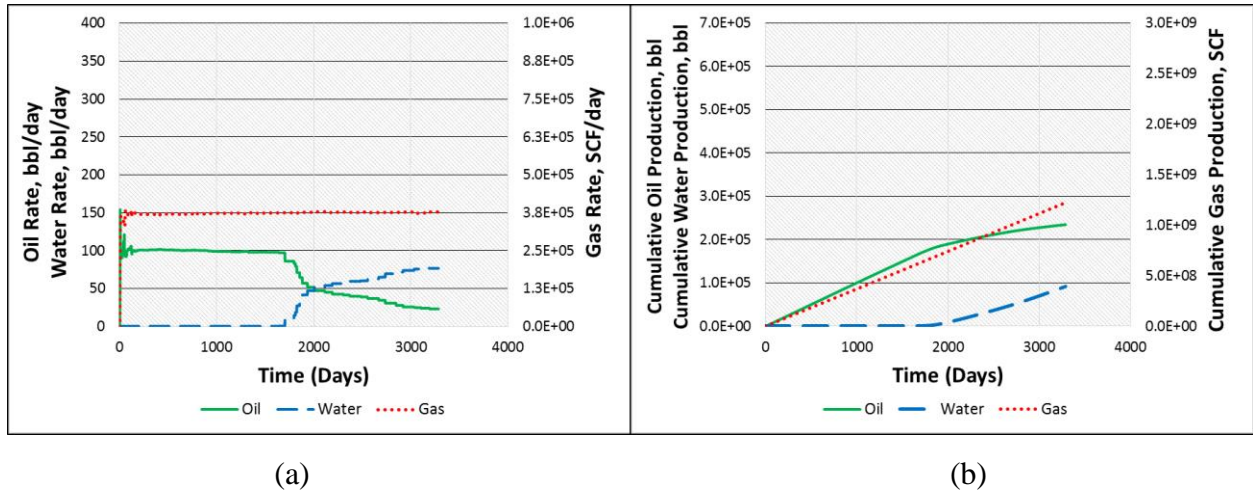


Fig. A7. Evaluation of supercritical CO₂ and surfactant solution co-injection (MRF = 100; scenario 3b in Table 3 with $f_g = 0.66$ and $q_t = 1572 \text{ ft}^3/\text{day}$ at reservoir condition): (a) production rates and (b) cumulative production (9 years)

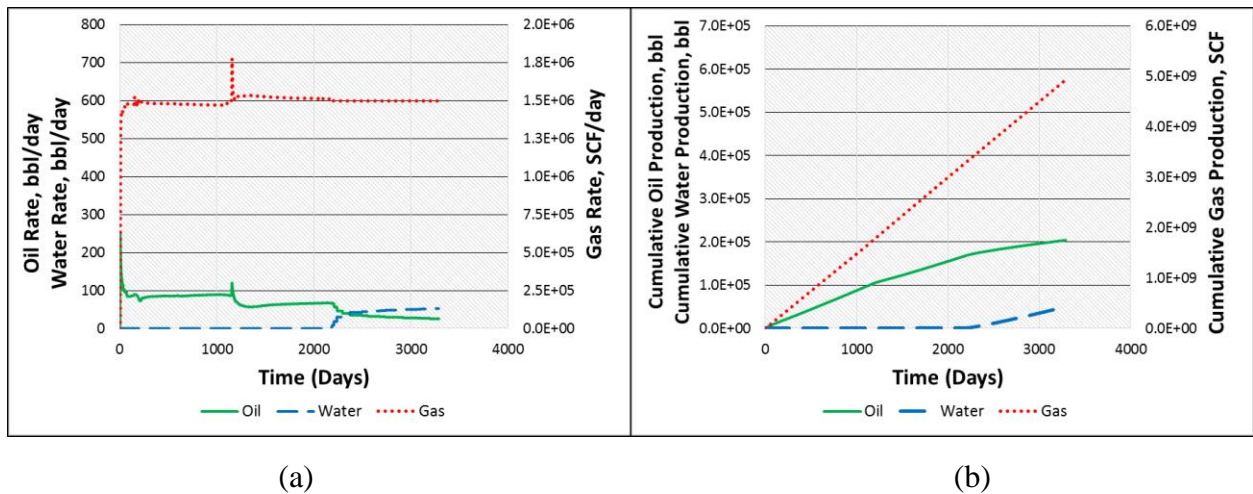


Fig. A8. Evaluation of supercritical CO₂ and water co-injection (MRF = 1 (no foam); scenario 4 in Table 3 with $f_g = 0.90$ and $q_t = 4379 \text{ ft}^3/\text{day}$ at reservoir condition): (a) production rates and (b) cumulative production (9 years)

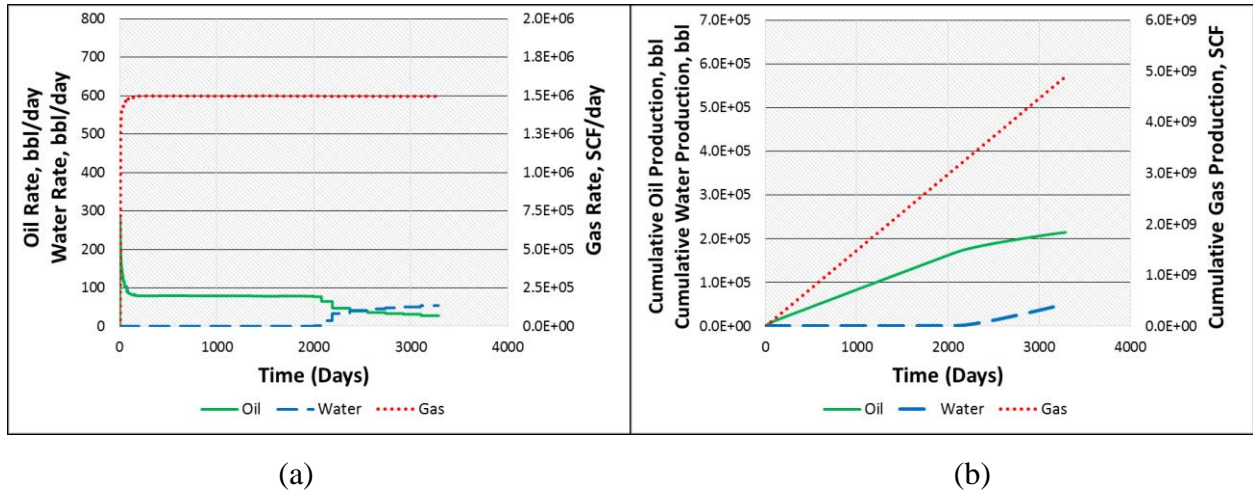


Fig. A9. Evaluation of supercritical CO₂ and nanoparticle solution co-injection (MRF = 10; scenario 4a in Table 3 with $f_g = 0.90$ and $q_t = 4379 \text{ ft}^3/\text{day}$ at reservoir condition): (a) production rates and (b) cumulative production (9 years)

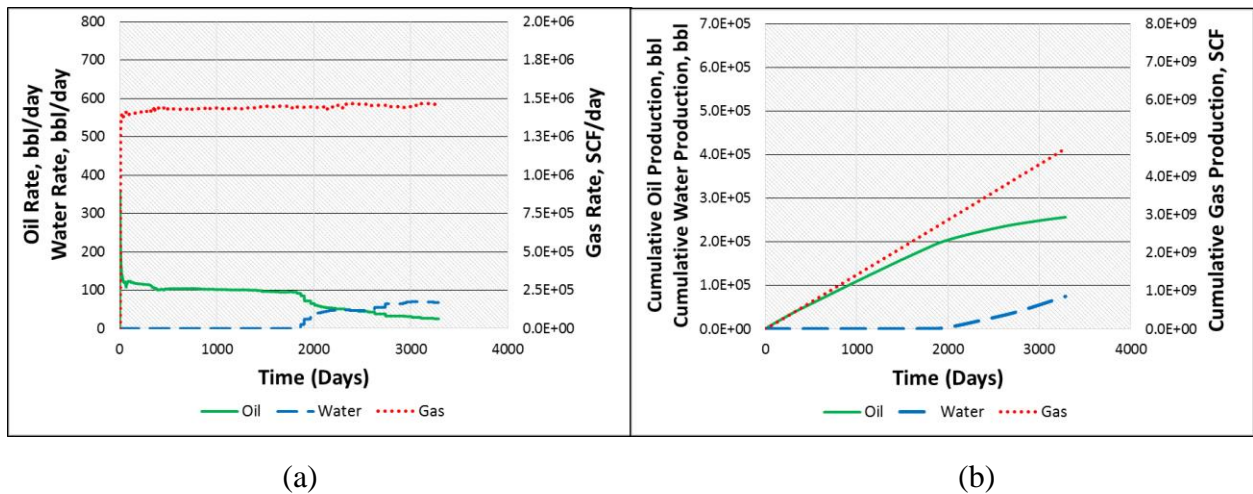


Fig. A10. Evaluation of supercritical CO₂ and surfactant solution co-injection (MRF = 100; scenario 4b in Table 3 with $f_g = 0.90$ and $q_t = 4379 \text{ ft}^3/\text{day}$ at reservoir condition): (a) production rates and (b) cumulative production (9 years)

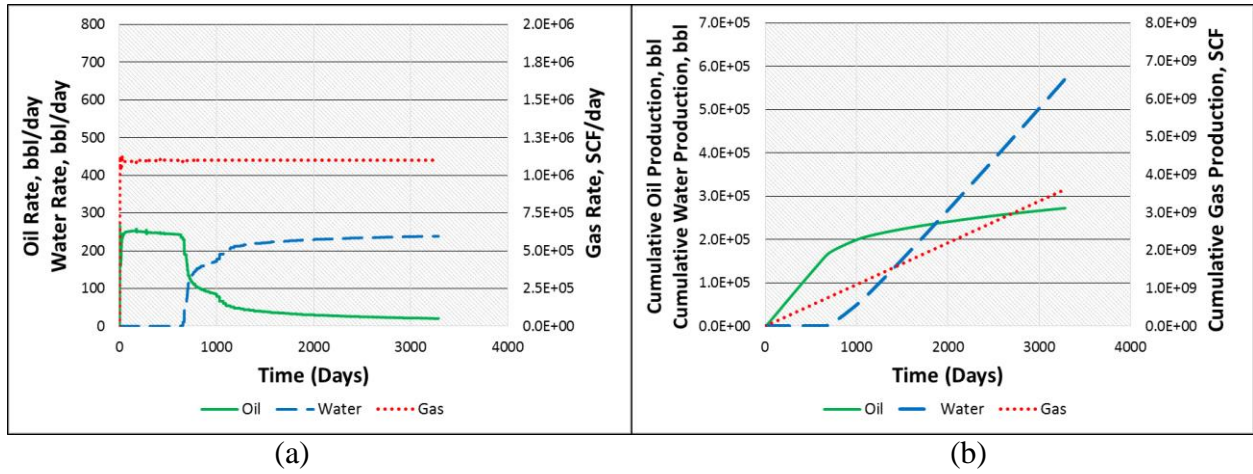


Fig. A11. Evaluation of supercritical CO₂ and water co-injection (MRF = 1 (no foam); scenario 5 in Table 3 with $f_g = 0.66$ and $q_t = 4379$ ft³/day at reservoir condition): (a) production rates and (b) cumulative production (9 years)

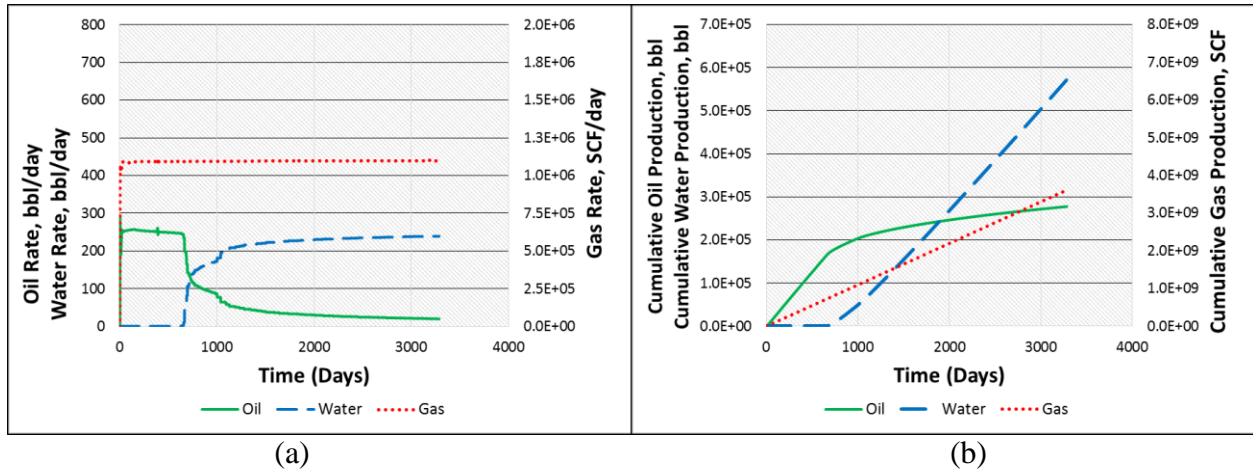


Fig. A12. Evaluation of supercritical CO₂ and nanoparticle solution co-injection (MRF = 10; scenario 5a in Table 3 with $f_g = 0.66$ and $q_t = 4379$ ft³/day at reservoir condition): (a) production rates and (b) cumulative production (9 years)

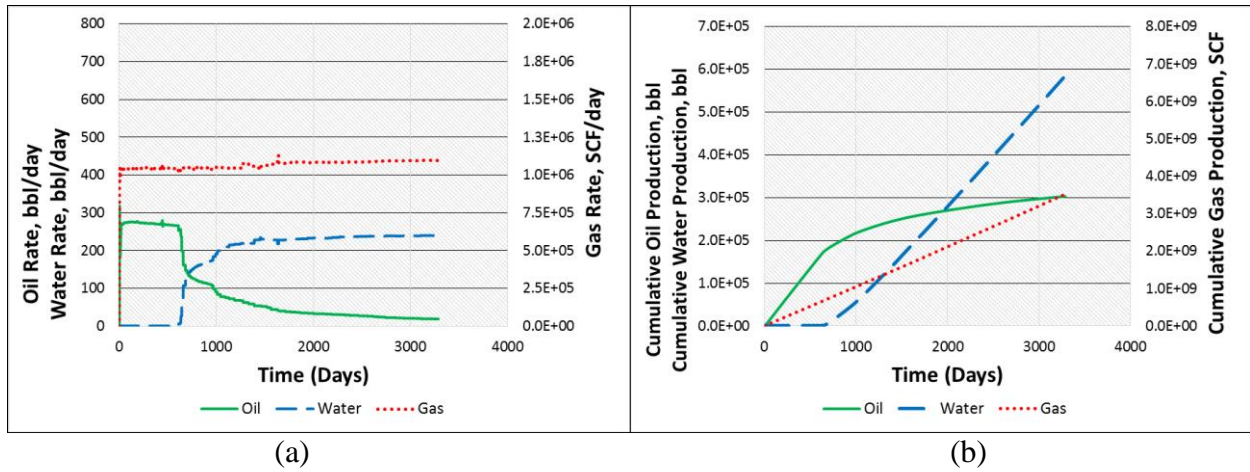


Fig. A13. Evaluation of supercritical CO₂ and surfactant solution co-injection (MRF = 100; scenario 5b in Table 3 with $f_g = 0.66$ and $q_i = 4379$ ft³/day at reservoir condition): (a) production rates and (b) cumulative production (9 years)

APPENDIX B

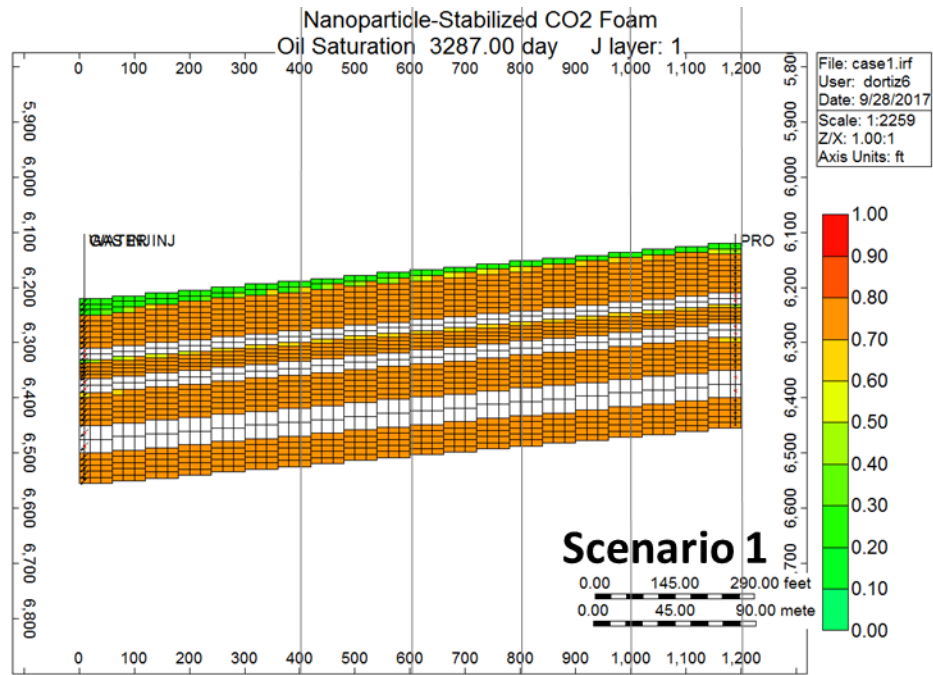


Fig. B1. Saturation profiles of scenario 1 in Table 3 with $f_g = 1$ and $q_t = 1572 \text{ ft}^3/\text{day}$ at reservoir condition

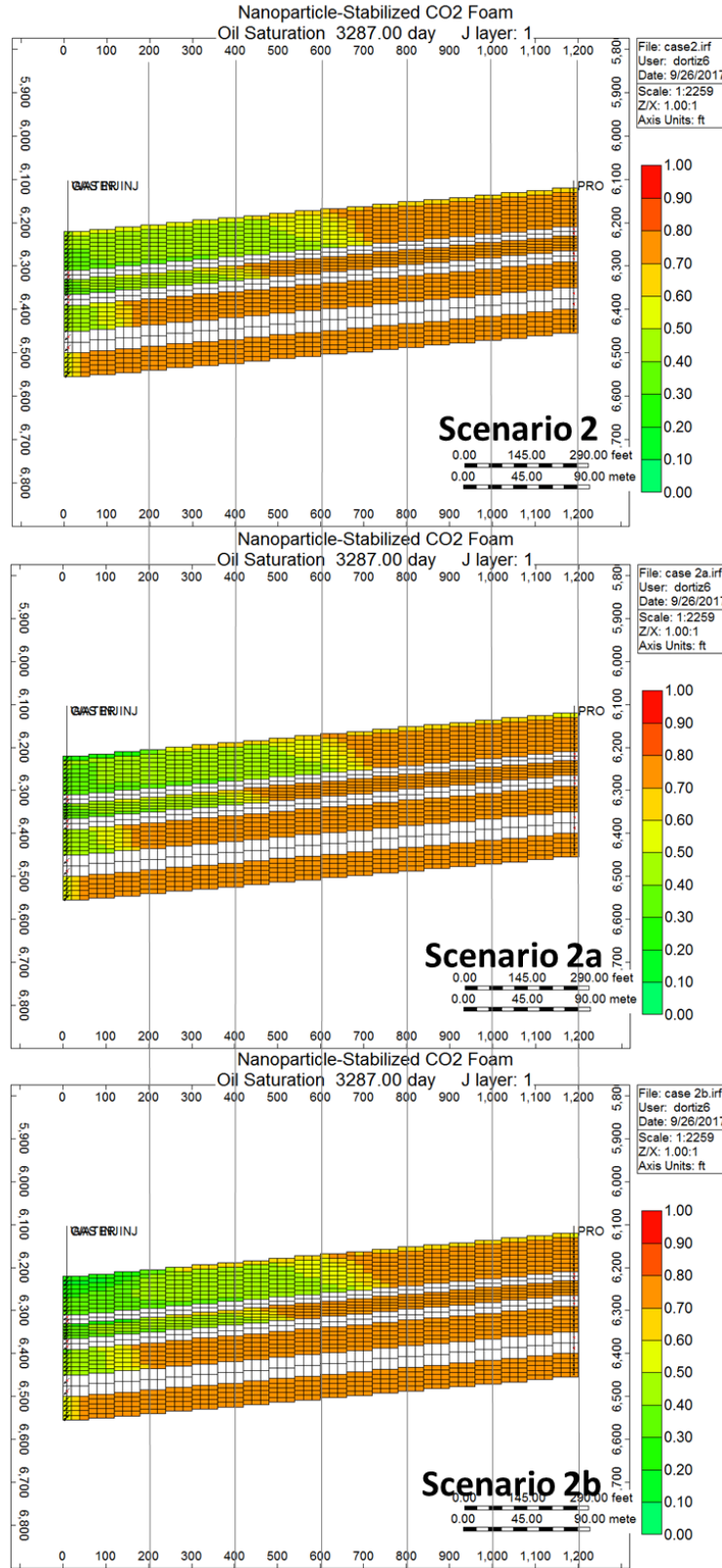


Fig. B2. Saturation profiles of scenarios 2 (no foam; MRF = 1), 2a (MRF = 10) and 2b (MRF = 100) in Table 3 with $f_g=0.90$ and $q_t=1572 \text{ ft}^3/\text{day}$ at reservoir condition

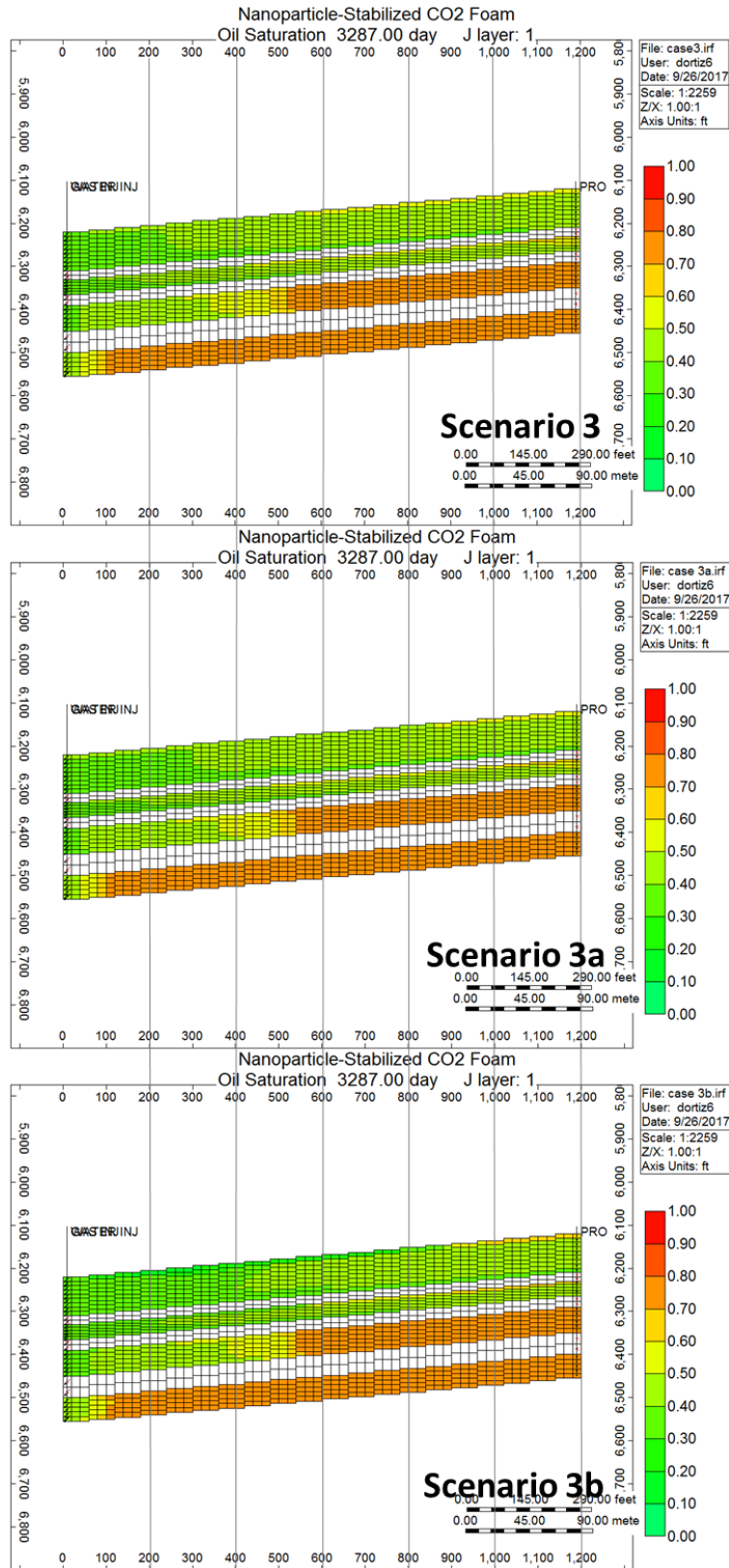


Fig. B3. Saturation profiles of scenarios 3 (no foam; MRF = 1), 3a (MRF = 10) and 3b (MRF = 100) in Table 3 with $f_g = 0.66$ and $q_t = 1572 \text{ ft}^3/\text{day}$ at reservoir condition

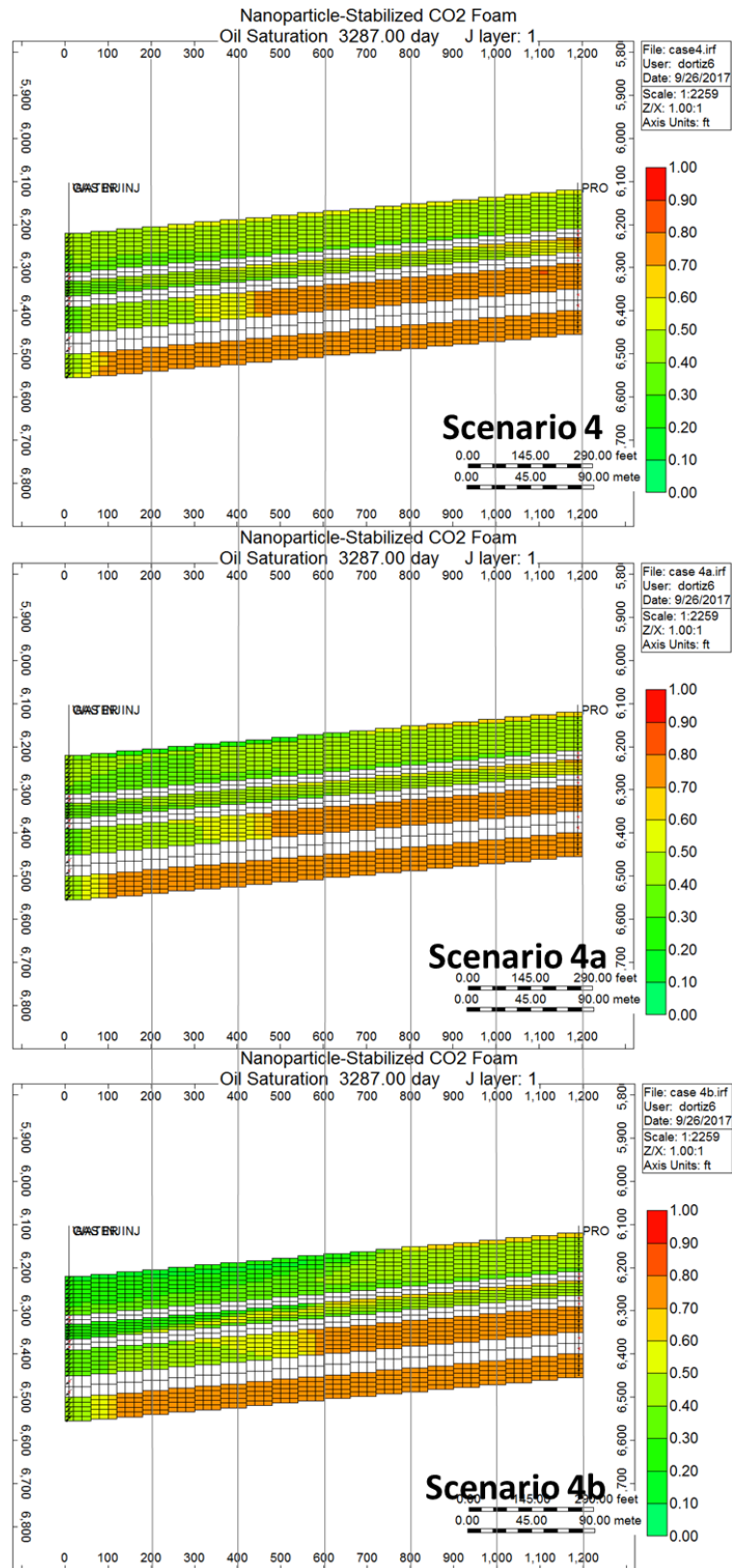


Fig. B4. Saturation profiles of scenarios 4 (no foam; MRF = 1), 4a (MRF = 10) and 4b (MRF = 100) in Table 3 with $f_g=0.90$ and $q_t=4379$ ft³/day at reservoir condition

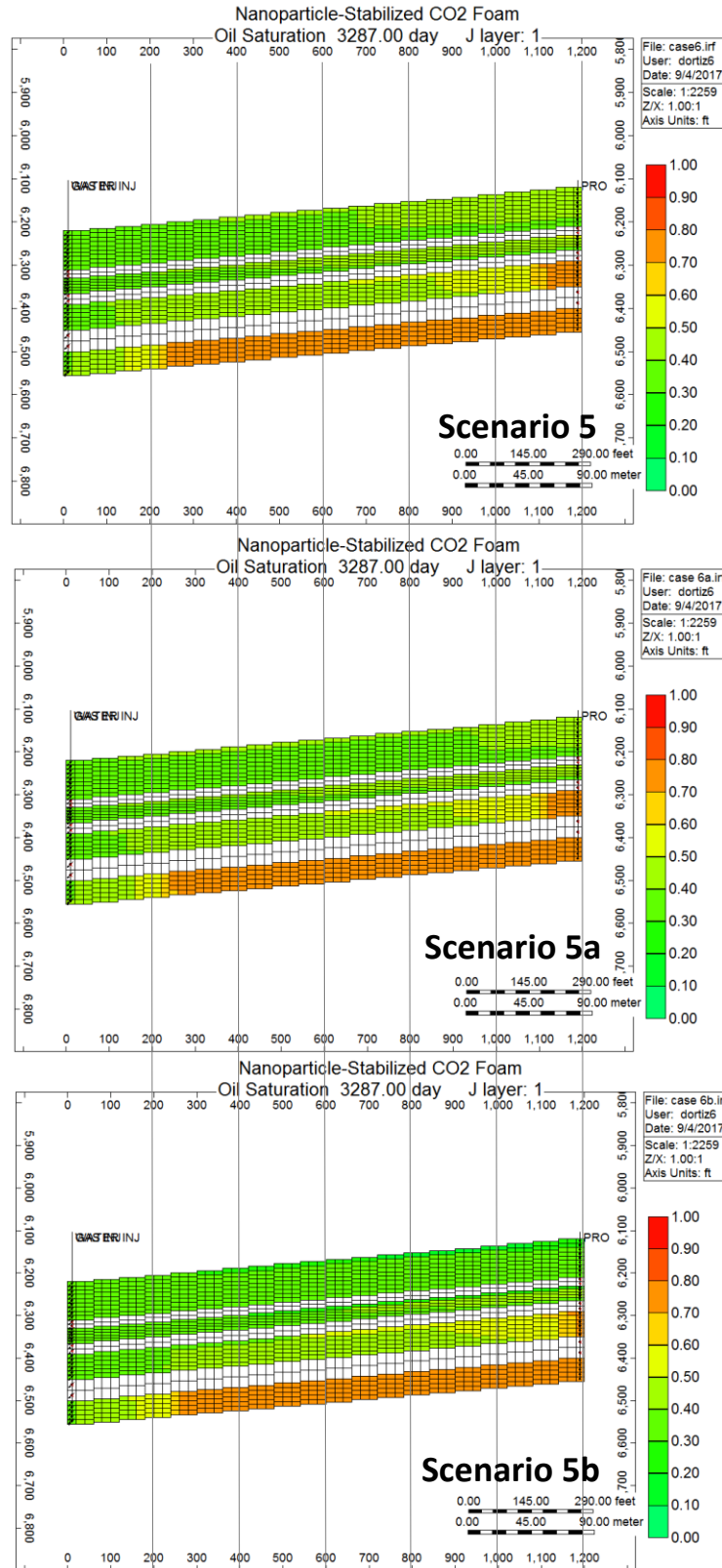


Fig. B5. Saturation profiles of scenarios 5 (no foam; MRF = 1), 5a (MRF = 10) and 5b (MRF = 100) in Table 3 with $f_g=0.66$ and $q_t=4379 \text{ ft}^3/\text{day}$ at reservoir condition

VITA

Doris Ortiz was born in Bogota, Colombia, on September 30, 1988. She received a Bachelor in Petroleum Engineering in 2010 from Universidad de America, Colombia. During her bachelor studies, she did an internship with the national oil company in Colombia, Ecopetrol, in la Cira Infantas field for five months. Also, in 2010, she was an intern at Schlumberger in the Casabe Alliance reservoir team for one year. After she obtained her engineering degree, she was hired in 2011 as a field engineer Production Technologist in Schlumberger to work with the reservoir and subsurface & surveillance teams for Casabe field. In 2016, she joined the Department of Petroleum Engineering at Louisiana State University as an M.S. candidate, and the Foam Injection EOR research group led by Dr. Seung Kam.